

Space Density of Optically-Selected Type 2 Quasars

Reinabelle Reyes¹, Nadia L. Zakamska^{2,3}, Michael A. Strauss¹, Joshua Green¹, Julian H. Krolik⁴, Yue Shen¹, Gordon T. Richards⁵, Scott F. Anderson⁶, Donald P. Schneider⁷

ABSTRACT

Type 2 quasars are luminous active galactic nuclei (AGN) whose central regions are obscured by large amounts of gas and dust. In this paper, we present a catalog of type 2 quasars from the Sloan Digital Sky Survey (SDSS), selected based on their optical emission lines. The catalog contains 887 objects with redshifts $z < 0.83$; this is six times larger than the previous version and is by far the largest sample of type 2 quasars in the literature. We derive the [OIII]5008 luminosity function for $10^{8.3}L_{\odot} < L_{[\text{OIII}]} < 10^{10}L_{\odot}$ (corresponding to intrinsic luminosities up to $M[2400\text{\AA}] \simeq -28$ mag or bolometric luminosities up to 4×10^{47} erg/sec). This luminosity function provides strong lower limits to the actual space density of obscured quasars, due to our selection criteria, the details of the spectroscopic target selection, as well as other effects. We derive the equivalent luminosity function for the complete sample of type 1 (unobscured) quasars; then, we determine the ratio of type 2/type 1 quasar number densities. Our best data constrain this ratio to be at least $\sim 1.5 : 1$ for $10^{8.3}L_{\odot} < L_{[\text{OIII}]} < 10^{9.5}L_{\odot}$ at $z < 0.3$, and at least $\sim 1.2 : 1$ for $L_{[\text{OIII}]} \sim 10^{10}L_{\odot}$ at $0.3 < z < 0.83$. Type 2 quasars are at least as abundant as type 1 quasars in the relatively nearby Universe ($z \lesssim 0.8$) for the highest luminosities.

Subject headings: surveys - galaxies: active - galaxies: quasars: general - galaxies: quasars: emission lines

1. Introduction

Unification models of active galactic nuclei (AGN) aim to explain the differences in the observed properties of AGN as orientation effects arising from the non-isotropic nature of obscuring material that surrounds the central engine (Antonucci 1993; Urry & Padovani 1995). These mod-

els are well-established for low-luminosity nearby AGN (Seyfert galaxies), but their applicability to the luminosities and redshifts of quasars has long been controversial. Type 2 quasars are luminous AGN whose central regions are obscured by large amounts of gas and dust; they are the more luminous analogs of high ionization narrow emission line (type 2) Seyfert galaxies. Type 2 quasars have been difficult to find because they are faint in the optical bands and because they are rare in the local Universe. Until recently, only a handful of candidates had been identified based on their unusual optical colors (Djorgovski et al. 2001), unusually hard X-ray spectra (Norman et al. 2002; Stern et al. 2002), and large far-infrared-to-optical ratios (Kleinmann et al. 1988).

The advent of large optical, X-ray and infrared (IR) surveys has enabled the construction of more substantial samples of type 2 quasars. Dozens of objects have been selected via their hard X-ray emission in *Chandra* and *XMM-Newton* fields (Szokoly et al. 2004; Barger et al. 2005; Brusa et al.

¹Princeton University Observatory, Peyton Hall, Princeton, New Jersey 08544.

²Institute for Advanced Study, Einstein Drive, Princeton, NJ 08540.

³Spitzer Fellow.

⁴Department of Physics and Astronomy, Johns Hopkins University, 3400 North Charles Street, Baltimore, MD 21218-2686.

⁵Department of Physics, Drexel University, 3141 Chestnut Street, Philadelphia, PA 19104.

⁶Astronomy Department, Box 351580, University of Washington, Seattle, WA 98195

⁷Department of Astronomy and Astrophysics, Pennsylvania State University, 525 Davey Laboratory, University Park, PA 16802, USA.

2007), and via their mid-IR colors in *Spitzer* fields (Lacy et al. 2004; Stern et al. 2005; Martínez-Sansigre et al. 2006; Lacy et al. 2007). Such samples are limited by the volume of their parent surveys, and furthermore all candidates require optical spectroscopic follow-up to confirm their classification.

Zakamska et al. (2003) (hereafter Paper I) utilized the large volume probed by the spectroscopic survey of the Sloan Digital Sky Survey (SDSS; York et al. 2000) to select hundreds of type 2 quasar candidates based on their optical emission lines. Multi-wavelength observations of the most luminous objects have confirmed that they have infrared luminosities up to and above 10^{46} erg s $^{-1}$, show the spectral energy distribution expected of type 2 quasars (Zakamska et al. 2004; Vignali et al. 2004; Ptak et al. 2006; Vignali et al. 2006; Zakamska et al. 2008a,b), and contain type 1 quasars in their centers revealed by polarimetric measurements (Zakamska et al. 2005, 2006).

In this paper, we employ the same promising selection technique on the latest SDSS data to expand the sample of optically-selected type 2 quasars. We present the largest sample of type 2 quasars to date, with 887 objects in the redshift range $z \leq 0.83$ with luminosities extending to $L_{[\text{OIII}]} \gtrsim 10^{10} L_{\odot}$ (corresponding to intrinsic UV luminosity $M_{2400} \lesssim -28$ mag). We then use this sample to calculate the luminosity function of type 2 quasars. Quantifying the obscured quasar population is essential for many applications, such as relating the present mass density of local black holes to the accretion history of the entire AGN population (e.g., Soltan 1982; Yu & Tremaine 2002; Marconi et al. 2004), understanding the origin of the cosmic X-ray background (e.g., Comastri et al. 1995; Gilli et al. 2007), and studying the effects of luminosity on AGN structure (e.g., Lawrence 1991; Urry & Padovani 1995; Hopkins et al. 2006).

From optical surveys, it has long been known that obscured AGN dominate the low-luminosity AGN population in the local Universe (Osterbrock & Shaw 1988; Salzer 1989; Huchra & Burg 1992). More recently, Hao et al. (2005b) and Simpson (2005) used the SDSS galaxy sample to determine the luminosity function of type 2 AGN at $z \sim 0.1$. They found that type 2 AGN make up about 60% of the AGN population at $L_{[\text{OIII}]} \sim 10^6 L_{\odot}$, and

about 30% at $\sim 3 \times 10^7 L_{\odot}$.

Results from hard X-ray (2-10 keV) selected samples suggest that the fraction of obscured quasars is large ($\gtrsim 50\%$) at low luminosities, but then decreases at higher luminosities (Ueda et al. 2003; Szokoly et al. 2004; Barger et al. 2005; Markwardt et al. 2005; Treister et al. 2006; Beckmann et al. 2006; Sazonov et al. 2007). All type 2 quasar candidates have to be confirmed by optical spectroscopy, which limits the completeness of X-ray selected samples. Additionally, X-ray surveys may be missing Compton-thick objects which might constitute a significant fraction of all AGN (Heckman et al. 2005; Polletta 2006; Martínez-Sansigre et al. 2007).

Since all emission absorbed by the circumnuclear material is ultimately thermally re-emitted in mid- and far-IR, selection of obscured quasars from infrared observations is a promising technique (Lacy et al. 2005; Stern et al. 2005; Martínez-Sansigre et al. 2006; Polletta et al. 2007). Currently, it is restricted by small sample sizes, poorly-understood selection effects and the requirement of optical or IR spectroscopic follow-up of the candidates. Martínez-Sansigre et al. (2006) estimated the fraction of obscured quasars at $z \sim 2$ to be $\sim 70\%$, higher than the fraction derived from X-ray selected samples, but their analysis is based on a small sample of moderately radio-bright objects. From another small sample of type 2 quasars with Si absorption Polletta et al. (2007) estimated the fraction of obscured quasars to be 60 – 65% at bolometric luminosities 10^{46-47} erg s $^{-1}$, but this sample excludes type 2 quasars with featureless IR spectra (Sturm et al. 2006). The obscured quasar fraction can also be determined by calculating the fraction of the total light emitted by obscuring material in the IR in type 1 AGN (Keel et al. 1994; Treister et al. 2007). Using this method, Treister et al. (2007) found type 2/type 1 ratios consistent with, but generally larger than, those derived from X-ray selected samples.

In this paper, we determine the obscured quasar fraction in the local Universe directly from the number counts of optically-selected type 1 and type 2 quasars. This is the first time that high-luminosity ($L_{[\text{OIII}]} \gtrsim 10^{10} L_{\odot}$) obscured quasars have been sampled in large enough numbers to allow this calculation. Our analysis provides lower limits to the space density of the obscured quasar

population, since there may be objects that are not included in our sample. For example, up to 20% of hard X-ray selected AGN do not show any emission lines in their optical spectra (Rigby et al. 2006) and therefore would not be included in our calculation. Likewise, partially extinguished ($A_V \lesssim 5$ mag) sources may constitute a significant fraction of the AGN population (Brand et al. 2007), but such objects show broad components in their permitted lines and would also be excluded by our selection procedure. On the other hand, our sample would include Compton-thick objects that are missed in X-ray surveys, as long as their optical spectra meet our selection criteria. Our results are thus independent of, and complementary to, those obtained from other studies.

The paper is structured as follows. In §2, we discuss our selection of type 2 quasars based on their optical emission lines and in §3, we determine the [OIII]5008 luminosity function from this sample. In §4, we determine the equivalent luminosity function from a complete sample of type 1 quasars and in §5, we determine the ratio of type 2 to type 1 quasars using the derived luminosity functions. We discuss implications of these results in §6 and we conclude in §7. Throughout the paper, we adopt a ‘concordance’ cosmology, $h = 0.7$, $\Omega_M = 0.3$, and $\Omega_\Lambda = 0.7$, identify emission lines using vacuum wavelengths, and identify objects with J2000 coordinates.

2. Type 2 Quasar Sample

Our sample of type 2 quasars is selected from the SDSS spectroscopic database as objects with high ionization, narrow emission lines, following Paper I. We describe SDSS data processing in §2.1, the targeting of objects for spectroscopy in the SDSS in §2.2, our spectroscopic selection criteria in §2.3 and [OIII]5008 luminosity measurements in §2.4.

2.1. SDSS Data

The SDSS uses a drift-scanning imaging camera (Gunn et al. 1998) and a pair of 320 fiber double spectrographs on a dedicated 2.5 m telescope (Gunn et al. 2006). The survey has imaged $\sim 10,000$ sq. deg. of the sky in the SDSS *ugriz* filters (Fukugita et al. 1996; Stoughton et al. 2002) and has obtained spectra of 1.3×10^6 objects, including

$\sim 8 \times 10^5$ galaxies and $\sim 10^5$ quasars (Adelman-McCarthy et al. 2007b). The astrometric calibration is accurate to better than $0''.1$ rms per coordinate (Pier et al. 2003), and the photometric calibration (Tucker et al. 2006; Smith et al. 2002) is accurate to 2% or better (Ivezić et al. 2004; Padmanabhan et al. 2007). For each object the photometric pipeline returns various measures of flux in each band, such as Petrosian (1976), point spread function (PSF) and model magnitudes (Stoughton et al. 2002). Throughout the paper, we use *asinh* magnitudes (Lupton et al. 1999) corrected for Galactic extinction (Schlegel et al. 1998).

A subset of objects from the imaging survey are targeted for spectroscopy, including galaxies (Strauss et al. 2002; Eisenstein et al. 2001) and quasars (Richards et al. 2002). The spectroscopic targets are assigned to a series of plates containing 640 fibers each (Blanton et al. 2003), each of which subtends $3''$ on the sky; the spectra cover $3800 - 9200 \text{ \AA}$ with resolution of $1800 < R < 2100$ and sampling of $\simeq 2.4$ pixels per resolution element. The relative and absolute spectrophotometric calibration are good to $\sim 5\%$. Spectral flux errors per pixel are typically of the order $1 \times 10^{-17} \text{ erg s}^{-1} \text{ cm}^{-2} \text{ \AA}^{-1}$. These data have been made publicly available in a series of data releases; the most recent of these is Data Release 6 (DR6; Adelman-McCarthy et al. 2007b).

Two independent spectral reduction pipelines assign redshifts and classifications to these spectra. The `spectro1d` pipeline (Stoughton et al. 2002; Subbarao et al. 2002), fits Gaussian profiles to emission lines to determine emission-line redshifts, and the `specBS` pipeline, written by D. Schlegel, carries out χ^2 fits of spectra to templates in wavelength space. The pipelines also measure fluxes of several major emission lines ($H\alpha$, $H\beta$, [OII]3729, [OIII]4960, 5008, [NII]6550, 6585, MgII 2800). For 98% of spectra, the measured redshifts from the two pipelines agree within 300 km s^{-1} for galaxies, and 3000 km s^{-1} for quasars (Adelman-McCarthy et al. 2007b); some type 2 quasars are among the 2% of the discrepant objects and we have to treat them separately (§2.3).

2.2. SDSS Spectroscopic Target Selection

Spectroscopic target selection in the SDSS is based on a combination of photometric properties, such as magnitudes, colors, and morphologies, and

in some cases radio and X-ray properties. In this section, we describe the spectroscopic target algorithms important for selecting type 2 quasars.

Roughly 75% of all SDSS spectra are part of the Main survey, designed to produce close to complete samples of galaxies and quasars. Galaxies are targeted as resolved sources down to a limiting Petrosian magnitude of $r = 17.77$ (Strauss et al. 2002) and represent about 62% of objects in the Main survey. Luminous red galaxies (LRGs) are targeted based on their distinctive colors down to a Petrosian magnitude of $r = 19.5$ (Eisenstein et al. 2001) and represent 9% of the Main survey. The Low- z QSO algorithm targets mostly UV excess sources down to $i_{\text{PSF}} = 19.1$, and the High- z QSO algorithm targets point sources with the colors of high-redshift ($z > 3$) quasars down to $i_{\text{PSF}} = 20.2$ (Richards et al. 2002). Taken together, quasar candidates represent 13% of the Main survey.

Other Main survey target algorithms are assigned spectroscopic fibers only after the galaxy and quasar targets have been allocated, so they do not produce complete samples. Objects with unusual colors, radio emission detected by the FIRST survey (‘Serendipity FIRST’; Becker et al. 1995), and X-ray emission detected by the ROSAT survey (‘ROSAT’; Voges et al. 1999, see also Anderson et al. 2007) are selected down to a fiber magnitude of $i = 20.5$ (Stoughton et al. 2002). These so-called ‘serendipity’ targets constitute about 5% of the Main survey.

Another 10% of spectra are taken in the Equatorial Stripe of the Southern Galactic Cap, covering $\sim 300 \text{ deg}^2$, as part of the Special Southern survey (Adelman-McCarthy et al. 2006). Spectroscopic targeting algorithms for this survey are somewhat different from those in the Main survey. Those important for selection of type 2 quasars are: (i) modified versions of the Main survey algorithms, which target galaxies and quasars down to $\lesssim 1 \text{ mag}$ fainter limiting magnitudes, (ii) the ‘faint quasars’ algorithm, which is a modified version of the Main Low- z QSO algorithm with looser color criteria, and (iii) the ‘photoz’ algorithm, which targets sources in the blue end of the normal galaxy distribution down to a Petrosian r -band magnitude of 17.77. Special Southern survey algorithms are exploratory in nature and have changed several times over the course of the survey. For this reason, we do not use them in our calculation

of the luminosity function.

2.3. Spectroscopic Selection of Type 2 Quasars

Following Paper I, we select Type 2 quasars as objects with narrow emission lines without underlying broad components and with line ratios characteristic of non-stellar ionizing radiation. We searched the entire SDSS spectroscopic database as of 2006 July, which contains 1.08×10^6 spectra from 1770 plates, before accounting for duplicates. This corresponds to $\sim 80\%$ of the DR6 spectroscopic database (Adelman-McCarthy et al. 2007b), and is a three times larger sample than that in Paper I.

We carried out the selection using the spectrophotometric calibration used in the First Data Release (Abazajian et al. 2003). The Second Data Release paper (Abazajian et al. 2004) describes a substantial improvement in the spectrophotometric calibration algorithm, which affects the ratios of line strengths between the red and the blue end of the spectrum. There was an additional improvement in the algorithm incorporated in the Sixth Data Release (Adelman-McCarthy et al. 2007b), whereby spectra are calibrated relative to PSF rather than fiber magnitudes of the standard stars measured on each plate. Thus, the flux scale used in our luminosity calculations (§2.4 and §4.2) is 38% higher than what was used in the initial selection. These changes in calibration cause some minor incompleteness at the faint end of the luminosity function, but very few objects change their classification from AGN to star forming galaxy (Eqs. 1-3 below) due to these changes.

Our automated selection algorithm applies a redshift cut, a signal-to-noise ratio cut on the spectra, an [OIII]5008 luminosity cut, and a set of emission line ratio cuts. The resulting ~ 4000 spectra are then visually inspected and fit for broad components in $\text{H}\beta$ and $\text{H}\alpha$ for final selection.

The major differences in our selection algorithm from that in Paper I are: (i) we now impose a luminosity cut, $L_{[\text{OIII}]} \geq 10^{8.3} L_{\odot}$, because selection based on emission line ratios becomes incomplete and noisy at low luminosities; (ii) we consider all objects with redshifts $z < 0.83$ (our previous sample was at redshifts $0.3 < z < 0.83$, complemented

by the $z < 0.3$ AGN samples by Hao et al. 2005a and Kauffmann et al. 2003); and (iii) we use an improved algorithm for identifying weak broad components in $H\alpha$ and $H\beta$ (Fig. 1 and text below).

We restrict the selection to objects with redshifts $z < 0.83$ so that the [OIII]5008 line (the strongest expected emission line) is present in all spectra. In order to select emission-line objects, we require the rest-frame equivalent width of [OIII]5008 to be $> 4\text{\AA}$. In addition, the signal-to-noise ratio must be ≥ 7.5 , where the signal is the flux density in the seventh brightest pixel over the entire spectroscopic range (3800-9200 \AA ; about 3840 pixels) and the noise is the median estimated flux error per pixel over all pixels. This unconventional criterion allows us to keep objects with weak continua but strong narrow emission lines, while rejecting continuum-dominated sources with low signal-to-noise ratio (Paper I).

When the redshift and classification of the two reduction pipelines `spectroid` and `specBS` (described in §2.1) agree, we apply different emission line criteria depending on the redshift of the object. For objects with redshifts $z < 0.36$, both $H\beta$ + [OIII]4960,5008 and $H\alpha$ + [NII] 6550,6585 line complexes are covered by the spectroscopic data, and the classical emission line diagnostic diagrams (Baldwin et al. 1981; Veilleux & Osterbrock 1987; Osterbrock 1989) are used to distinguish between a stellar and an AGN ionizing continuum. The MgII 2800 emission doublet is either not covered by the spectrum or falls into the UV where the spectra have low signal-to-noise ratio, so this line is not used for this group of spectra. We use line diagnostic criteria of the form suggested by Kewley et al. (2001) to distinguish type 2 quasars from star-forming galaxies and narrow-line Seyfert galaxies. We require the ratio of luminosities $\mathcal{R} \equiv [\text{OIII}]5008/H\beta$ to satisfy either:

$$\log(\mathcal{R}) > \frac{0.61}{\log([\text{NII}]6585/H\alpha) - 0.47} + 1.19 \quad (1)$$

or

$$\log(\mathcal{R}) > \frac{0.72}{\log([\text{SII}]/H\alpha) - 0.32} + 1.30, \quad (2)$$

where [SII] refers to the combined luminosity of the doublet [SII]6718,6733.

For objects with redshifts $0.36 \leq z < 0.83$, the $H\alpha$ + [NII] line complex is not covered by the SDSS

spectra, so the classical diagnostic diagrams cannot be used. We adopt the [OIII]5008/ $H\beta$ ratio requirement in reduced form:

$$\log(\mathcal{R}) > 0.3, \text{ if } H\beta \text{ is detected with } S/N > 3 \quad (3)$$

or we require that $H\beta$ is undetected, while [OIII]5008 is detected. In addition, for $z > 0.6$, the full width at half maximum (FWHM) of MgII 2799 is required to be < 2000 km/s.

In the 2% of cases for which the two spectroscopic reduction pipelines do not agree on redshift or classification, we find the emission line closest to the expected position of [OIII]5007, given either of the two redshifts. If the line satisfies the appropriate equivalent width and luminosity criteria above, we keep the object as a candidate.

These selection criteria are designed to be maximally inclusive. In particular, the line diagnostic criteria given in Eqs. 1 and 2 are applied with the ‘OR’ operator, in case some of the lines are not measured properly. At redshifts $z > 0.36$, only a very mild line ratio cut (Eq. 3) is imposed. Apart from the MgII 2800 width criterion on $z > 0.6$ objects, no criteria to explicitly reject broad-line AGN are imposed at this selection stage, since the weak $H\beta$ lines common in type 2 AGN are often poorly measured by the spectroscopic pipelines. Nevertheless, the vast majority of type 1 AGN are easily rejected by the automated procedure; because of their broad $H\alpha$ and $H\beta$, they tend to have small values of $\log([\text{OIII}]5008/H\beta)$, $\log([\text{NII}]6585/H\alpha)$ and $\log([\text{SII}]6718,6733/H\alpha)$, making these objects fail the line diagnostic criteria given in Eqs. 1 and 2. This automated procedure selected $\sim 4,000$ objects for visual inspection.

At the visual inspection stage, we pursue two goals: (i) to remove objects with broad components in their permitted emission lines (the major contaminant at $z < 0.36$); (ii) to reject star-forming galaxies (the major contaminant at $z \geq 0.36$, since at $z < 0.36$ the diagnostic diagrams are robust). We consider the [NeV] 3347, 3427 emission lines to be unambiguous signs of an underlying AGN continuum (Groves et al. 2004; Nagao et al. 2006), so if either one of these lines is detected (if a single line is detected, it is usually [NeV] 3427), the object is considered an AGN. If neither of the [NeV] lines is detected, we use the

criterion $\text{FWHM}([\text{OIII}] 5008) > 400 \text{ km/s}$ as a sign of AGN activity (Zakamska et al. 2003; Hao et al. 2005a). Since the [NeV] lines are weak, our selection is more robust at high luminosities, where these lines are more likely to be detected.

Objects identified as AGN are then checked for broad lines. The broad component in the $\text{H}\beta$ line can be rejected by examining the difference in χ^2 of a single Gaussian and a double Gaussian fit to this line, similar to Hao et al. (2005a). However, identifying weak broad components in $\text{H}\alpha$ is complicated by the non-Gaussianity of emission lines and blending with [NII] 6550, 6585. Thus, we do not automatically reject objects for which a four-Gaussian fit is statistically preferred to a three-Gaussian fit to the $\text{H}\alpha$ + [NII] line complex. Instead, we use the non-parametric line fitting procedure illustrated in Figure 1. First, we derive narrow line profiles from the [OIII]4960, 5008 emission lines, and then fit the $\text{H}\alpha$ + [NII] complex assuming that all three lines have the same profile (with the ratio [NII]6585/[NII]6550 fixed to be equal to 3). We visually examine the residuals, and if the non-parametric fit can reproduce the width of the complex, we keep the object in our sample.

This selection procedure results in the sample of 887 type 2 quasars given in Table 1. Figures 2 to 4 show sample spectra of high [OIII]5008 luminosity objects in our sample, in order of increasing redshift. More than 90% of the type 2 quasar candidates selected in Paper I are recovered by the automated selection procedure described above, so we estimate that roughly the same percentage of type 2 quasars in the SDSS database are successfully selected. The spectra of those objects from Paper I that we did not recover tend to be of low signal-to-noise ratio or have ambiguous classification.

2.4. Measurement of [OIII]5008 Luminosities

We measure [OIII]5008 luminosities from spectra calibrated with the most recent spectrophotometric calibration algorithm (Adelman-McCarthy et al. 2007b and §2.3), and we do not correct the measured line luminosities for dust extinction (§6.2). Since FeII emission tends to be negligible in type 2 quasars (unlike in type 1 quasars, for which we carefully subtract FeII emission to

measure [OIII]5008 luminosities in §4.2), we fit the [OIII]4960,5008 lines with two Gaussians of the same width and a fixed 1 : 3 amplitude ratio, plus a linear continuum, over the wavelength range 4860Å to 5060Å. The [OIII]5008 luminosity is then calculated using the luminosity distance as a function of redshift (e.g., Hogg 1999).

To check the fits, we also obtain a non-parametric measure of the [OIII]5008 line luminosity by integrating the detected flux density and subtracting the continuum contribution. As Fig. 1 shows, this line is often significantly non-Gaussian, especially at its base. Asymmetries in line profiles, thought to be caused by radial outflows in the narrow-line region, have been observed in many AGN (Heckman et al. 1981; Whittle 1985). We find that the non-parametric measure of the luminosity is systematically larger, by 5% on average, than the Gaussian measure; this indicates the presence of non-Gaussian wings in the [OIII]5008 profiles of objects in our sample.

Both Gaussian and non-parametric measures are given in Table 1. In the rest of the paper, $L_{[\text{OIII}]}$ refers to luminosities measured from Gaussian fits. About 30% of the sample (257 objects) have $L_{[\text{OIII}]} > 10^{9.5} L_{\odot}$. As we explained in §2.3, the luminosity cut we have imposed in our selection, $L_{[\text{OIII}]} > 10^{8.3} L_{\odot}$, was applied to luminosities calibrated using a flux scale that is $\sim 38\%$ lower than the one we use for these line measurements. Due to this change in spectrophotometric calibration, there are 149 objects with measured [OIII]5008 luminosities below $10^{8.3} L_{\odot}$; of these, 79% are within 30% of this value.

3. Type 2 Quasar Luminosity Function

In this section, we derive the [OIII]5008 luminosity function (LF) from our sample of type 2 quasars. Since type 2 quasars are heavily obscured, the optical continuum luminosity is by definition a poor indicator of their bolometric luminosity. We use the [OIII]5008 emission line as a proxy of the AGN activity, since it is emitted from the extended narrow-line region and can serve as a tracer of AGN bolometric luminosity for both type 1 and type 2 quasars. Hao et al. (2005b) and Simpson (2005) derived the [OIII]5008 luminosity function from a sample of type 2 AGN with redshifts $z \lesssim 0.3$ and [OIII]5008 luminosities up to

$\sim 10^{8.6}L_{\odot}$ and $= 10^{8.9}L_{\odot}$, respectively. Our sample probes redshifts up to $z = 0.83$ and [OIII]5008 luminosities up to $\sim 10^{10}L_{\odot}$. To minimize the systematic effect of redshift evolution within the sample, we present the LF for three ranges in redshift: $z \leq 0.30$, $0.30 < z \leq 0.50$ and $0.50 < z \leq 0.83$.

The type 2 quasar LF we derive is a lower limit to the true LF for several reasons. First, there may be a substantial population of obscured quasars whose emission lines do not meet our selection criteria, so they are not included in our sample. Second, there may be objects that fall outside the regions in the multi-dimensional parameter space of colors, magnitudes and morphologies, which the SDSS spectroscopic target algorithms are designed to target, so they are also not included in our sample. Third, we use line luminosities that are not corrected for reddening (§6.2; such a correction would shift the LF toward higher luminosities and would yield a higher space density at any given luminosity.

In §3.1 and §3.2, we discuss the calculation of the LF, and in §3.3, we present the results and compare it with previous work. The derived type 2 quasar LF is shown in Fig. 7. In §3.4, we discuss the efficiency of our selection of type 2 quasars and its implications to the interpretation of the derived LF.

3.1. $1/V_{\max}$ Luminosity Function

We use the $1/V_{\max}$ LF estimator (Schmidt 1968), in which the contribution of each object to the luminosity function is weighted by its available volume V_{\max} . To determine V_{\max} , we begin by noting that objects in our type 2 quasar sample are selected for spectroscopy by one or more of several algorithms, which we have briefly described in §2.2. Table 2 lists the algorithms that are important in selecting type 2 quasars, together with the number of objects targeted by each. An object can be targeted by multiple target algorithms, so these numbers do not add up to the total number of objects in the catalog.

In the calculation of the LF, we include only objects from the Main survey. Target algorithms of the Special survey have changed over time (Adelman-McCarthy et al. 2006), which is why we do not use objects from this survey. Furthermore, we include only objects targeted by any of the top

four Main survey algorithms (Galaxy, Low- z QSO, High- z QSO and Serendipity FIRST), which together represent 83% of the full catalog (740 objects). Fig. 5 shows the distribution of [OIII]5008 luminosities and redshifts of objects targeted by these algorithms.

In calculating V_{\max} , the line luminosity and S/N criteria we have applied in §2.3 are not important for the luminosity and redshift ranges we are interested in, since the [OIII]5008 line is strongly detected in all objects in our sample. We therefore focus on the selection criteria from the spectroscopic target selection. Therefore, for our purposes, V_{\max} is given by the comoving volume over which an object would be selected by any of the top four Main survey algorithms:

$$V_{\max} = \frac{\Omega}{4\pi} \int_{z_1}^{z_2} \Theta(z) \frac{dV_c}{dz}(z) dz, \quad (4)$$

where Ω is the effective survey area, z_1 and z_2 are the edges of the redshift range for which we are calculating the luminosity function, $(dV_c/dz)dz$ is the comoving volume element in the redshift interval dz (e.g., Hogg 1999), and $\Theta(z)$ is a generalized step function that is equal to zero if the object is not selected by any of the four algorithms we consider, and nonzero otherwise. We describe in detail how we calculate $\Theta(z)$ in §3.2.

The effective survey area Ω is given by the area covered by the Main survey plates from which we have selected objects. To calculate Ω , we define areas of intersection of plates and tiling rectangles and take the area covered by their union (see Appendix B of Shen et al. 2007 and references therein for details). This calculation yields $\Omega \approx 6293$ deg². Since some post-DR5 plates are included in our parent sample, this area is slightly bigger than the DR5 spectroscopic footprint area of 5740 deg² (Adelman-McCarthy et al. 2007a).

The $1/V_{\max}$ luminosity function and its uncertainty are then given by

$$\Phi(\bar{L}_k) = \frac{1}{(\Delta L)_k} \sum_{j=1}^{N_k} \left(\frac{1}{V_{\max,j}} \right) \quad (5)$$

and

$$\sigma(\Phi) = \frac{1}{(\Delta L)_k} \left[\sum_{j=1}^{N_k} \left(\frac{1}{V_{\max,j}} \right)^2 \right]^{1/2}, \quad (6)$$

where \bar{L}_k is the mean [OIII]5008 luminosity of objects in the k th luminosity bin ($L, L+(\Delta L)_k$), and the sum is over the N_k objects in that bin. Here, $V_{\max,j}$ is the comoving volume over which an object would have been included in the sample, given its physical properties and the sample selection criteria. Following common practice, we present our results in terms of the number of quasars per unit volume per logarithmic luminosity interval, $\hat{\Phi}(L) = (L/\log_{10} e)\Phi(L)$.

3.2. Calculation of $\Theta(z)$

In this section, we calculate the function $\Theta(z)$, which appears in the expression for V_{\max} given above (Eq. 4). We determine whether an object, with redshift z_{obs} , would be selected by any of the top four target algorithms, if it were placed at some other redshift z , based on its intrinsic spectral energy distribution (SED). For this object, $\Theta(z)$ is given by a generalized step function:

$$\Theta(z) = \begin{cases} 1 & \text{, if selected by any of } G, L, \text{ or } H \\ \alpha & \text{, if selected solely by } S \\ 0 & \text{, if not selected by } G, L, H, \text{ or } S \end{cases} \quad (7)$$

where G, L, H , and S stand for the Galaxy, Low- z QSO, High- z QSO, and Serendipity FIRST algorithms, respectively, and α is a numerical factor (smaller than 1) that weights the contribution of the radio-selected objects to the LF. We discuss the determination of α in §3.2.4. In practice, we determine $\Theta(z)$ in steps of redshift, from $z = 0.1$ to 0.8, separated by $\Delta z = 0.01$, and we approximate the integral in Eq. 4 as a sum over these redshift slices.

To determine $\Theta(z)$ for a given object, we calculate what its observed optical and/or radio properties would be if it were placed at redshift z , and apply the relevant selection criteria for each algorithm. We scale the object's observed magnitudes via the luminosity distance dimming relation (e.g., Hogg 1999). In addition, we apply k-corrections (Sandage 1961) based on the object's observed SDSS spectrum; this takes into account both the shape of the SED and the shifting of emission lines in and out of bandpasses. The latter effect is important because an emission line with equivalent width $\sim 100 \text{ \AA}$ contributes roughly 10% of the flux in a bandpass $\sim 1,000 \text{ \AA}$ wide, and objects in our sample have equivalent widths as large as $1,400 \text{ \AA}$

(Paper I). To calculate k-corrections for the SDSS u and z bands, we extrapolate the observed spectrum outside $\sim 3,000\text{--}10,000 \text{ \AA}$ to be flat in flux density; our results are not sensitive to this extrapolation.

3.2.1. Main Galaxy Target Algorithm

The galaxy algorithm targets objects that have Petrosian magnitude $r < 17.77$ mag, r band Petrosian half-light surface brightness $\mu_{50} \leq 24.5$ mag arcsec $^{-2}$, and satisfy a star/galaxy (unresolved/resolved) separation cut and a fiber magnitude cut (Strauss et al. 2002).

Since surface brightness changes only by a factor of ~ 3 throughout the redshift range probed by the Galaxy algorithm ($z \lesssim 0.3$; Fig. 5), and no object in the sample is close to the star/galaxy separation cut, the magnitude cut alone determines whether an object is selected. We consider an object to be selected by this algorithm if its scaled and k-corrected Petrosian r -band magnitude is brighter than 17.77 mag. We assume for simplicity that the spectral shape within the Petrosian aperture is the same as within the spectroscopic fiber.

3.2.2. Low- z QSO and High- z QSO Target Algorithms

Low- z QSO targets must have $15.0 < i_{\text{PSF}} < 19.1$ and satisfy various color criteria, i.e., they must be outliers from the $ugri$ stellar locus, have non-galaxy colors if they are extended, and not occupy any of several exclusion regions in color space designed to eliminate white dwarfs, A-type stars, and other contaminants (Richards et al. 2002). All UV excess sources ($u - g < 0.6$) that are not in the white dwarf exclusion region and satisfy the magnitude limits are also targeted.

The High- z QSO target algorithm is designed to recover quasars at redshifts beyond ~ 3.0 , as the Lyman break moves across the photometric bands with increasing redshift. High- z QSO targets must be point-like sources with $15.0 < i_{\text{PSF}} < 20.2$ (Richards et al. 2002). They must also be outliers in the $griz$ stellar locus, or occupy certain regions in the color space where high-redshift quasars are expected to lie.

To determine whether an object would be selected by these algorithms at a redshift z , we run

the scaled and k-corrected PSF magnitudes and errors in all bands through the final version of the QSO target selection code `v3_1_0` (Richards et al. 2002).

3.2.3. Serendipity FIRST Target Algorithm

Serendipity FIRST targets are sources that have fiber magnitudes $14.0 < g, r, i < 20.5$ and have counterparts in the FIRST catalog within $2''$ of the optical position. Radio sources are included in the FIRST survey catalog if they have peak 20 cm radio flux density $S_{20\text{cm}} > 5\sigma + 0.25$ mJy/beam and $S_{20\text{cm}} > 1$ mJy/beam, where σ is the local RMS noise in the field (Becker et al. 1995).

To calculate the fiber magnitude as a function of redshift, we use the azimuthally-averaged radial surface brightness profile (following Appendix B of Strauss et al. 2002) to calculate the light that would fall into the aperture at each redshift, neglecting the effect of seeing. To calculate the radio flux density as a function of redshift, we assume a power-law radio spectrum $F_\nu = A\nu^\beta$ with $\beta = -0.5$, following Zakamska et al. (2004). Most of our objects are point radio sources, so we approximate the redshift scaling of the peak flux density $S_{20\text{cm}}$ to be the same as the total flux $F_\nu \propto D_L^{-2}(z)(1+z)^{1+\beta}$, where $D_L(z)$ is the luminosity distance at redshift z .

Since most objects targeted by the Serendipity FIRST algorithm were selected in the i -band and because the volume corresponding to the bright limit is negligibly small, we consider an object to be selected by this algorithm if it satisfies both the i -band fiber magnitude faint limit and the radio flux limits.

3.2.4. Probability of Radio-detection

Only a fraction of the radio-selected targets are assigned fibers for spectroscopic observation. Thus, we assign a weighting factor $\alpha = N_O/N_T = 10,480/25,307 = 0.414$, where N_T is the total number of radio-selected targets in the spectroscopic survey covered in our selection, and N_O is the number of these targets with observed spectra. This is the factor that appears in Eq. 7.

About 30% of the objects included in our LF calculation are selected solely by the Serendipity FIRST algorithm; these objects do not have the

optical morphologies or colors that would allow them to be selected by the three other algorithms we consider. This implies that there exists a substantial population of radio-weak type 2 quasars with optical SEDs similar to these radio-selected sources that are not included in our sample.

This suggests an additional weighting factor $p_{\text{RD}}(z, L_{[\text{OIII}]})$, the probability that an object with a given redshift and [OIII]5008 luminosity has a FIRST catalog match (Becker et al. 1995) within $2''$ of its optical position. With this radio-detection correction, the weighting factor $\alpha = (N_O/N_T) \times p_{\text{RD}}(z, L_{[\text{OIII}]})$. In §3.3, we show the type II quasar LF calculated both with and without this correction.

The distribution of radio luminosities in AGN and the relation, if any, between optical and radio properties are the subjects of much debate (Ivezić et al. 2004 and references therein). Here, we determine $p_{\text{RD}}(z, L_{[\text{OIII}]})$ from our data alone. We use the radio properties of the objects in our sample that are selected by at least one non-radio method (539 objects) to predict how many objects the Serendipity FIRST algorithm has missed because they fall below the flux limit of the FIRST survey. In the following calculation, we assume that the distribution of radio luminosities of a population of type 2 quasars is independent of their optical colors and morphology, but may depend on their [OIII]5008 luminosity and redshift.

We aim to find a simple analytic functional form for $p_{\text{RD}}(z, L_{[\text{OIII}]})$ that best fits the available data. We define a statistic analogous to χ^2 to assess the goodness of the fit. For a bin j in the redshift-[OIII]5008 luminosity space, which contains N objects with redshifts and luminosities z_i and L_i ($i = 1 \dots N$) of which n are detected by FIRST, this statistic is given by

$$u = \frac{N(f - \bar{p})^2}{\bar{p}(1 - \bar{p})}, \quad (8)$$

where $f = n/N$ and $\bar{p} = \sum_i p_{\text{RD}}(z_i, L_i)/N$. In the limit of large N and small bins (so that $p_{\text{RD}} \simeq \text{const}$ within each bin), we show in the Appendix that u is distributed as χ^2 with one degree of freedom. Therefore, the central limit theorem can be applied to the sum of the values of u over all bins, and this value gives the probability that the given form of $p_{\text{RD}}(z, L_{[\text{OIII}]})$ fits the data. Importantly, this statistic is independent of the distribution of

objects in the z - $L_{[\text{OIII}]}$ plane which is strongly affected by selection effects.

We expect that the probability of radio detection decreases with redshift, since objects farther out are dimmer, and increases with luminosity. We tried several functional forms for p_{RD} thus motivated and varied their parameters to minimize the sum of u over all bins. Our best-fit function is given by

$$p_{\text{RD}}(z, L) = \frac{1}{1 + [z/(0.15 + 0.1(\log L/L_{\odot} - 8.0))^2]} \quad (9)$$

The comparison of observed FIRST detection rates with those calculated using this function is shown in Fig. 6. By visually examining the agreement between the observed detection rates and p_{RD} (using slices and projections in z - $L_{[\text{OIII}]}$ plane) we estimate that p_{RD} is determined to better than $\pm 10\%$ over most of the parameter space. Since $p_{\text{RD}}(z, L_{[\text{OIII}]}) \sim 1$ at low redshifts, as well as high $[\text{OIII}]5008$ luminosities, the correction to the LF from this factor is not important in these regimes.

3.3. Results

We derive the type 2 quasar luminosity function for three ranges in redshift $z \leq 0.30$, $0.30 < z \leq 0.50$ and $0.50 < z \leq 0.83$, using Eqs. 5 and 6, summed over 420, 175 and 145 objects, respectively. Results with and without correction for the probability of detection of radio-selected objects (§3.2.4) are shown in Fig. 7.

The flattening of the $0.30 < z \leq 0.50$ and $0.50 < z \leq 0.83$ LFs at low $[\text{OIII}]5008$ luminosities is due to the decreased sensitivity of all the target algorithms to low-luminosity objects at high redshifts, mainly because of their flux limits (see also §3.4). This incompleteness is partially mitigated by the radio-detection correction, but even this result is still strictly a lower limit. Therefore, for these redshift ranges, the most useful information from the derived LFs is provided by the highest luminosity bins. The trend is reversed for the $z \leq 0.30$ LF, where the most useful information is provided by the low luminosity bins, since these represent many detected objects (see also §3.4).

While the high luminosity end of the LFs seem to suggest a tentative trend toward increasing number densities with increasing redshifts, we can-

not make any conclusive statements because these are all lower limits. We return to the question of redshift evolution in the sample in §5.2, but it is difficult to disentangle the effects of incompleteness of the sample with that of redshift evolution, and we make no attempt to do so.

Our result extends the luminosity function of optically-selected type 2 AGN. Figure 8 shows the high-luminosity end of the LF derived by Hao et al. (2005b) for the redshift range $z \leq 0.30$, using objects selected from the SDSS Main Galaxy spectroscopic database. We find good agreement with our derived type 2 quasar LF for the overlapping redshifts and luminosities. The luminosities of Hao et al. (2005b) had been shifted up by 0.14 dex to account for the difference in their spectrophotometric flux calibration (see §2.3). A more recent measurement of the type 1 AGN $\text{H}\alpha$ LF by Greene & Ho (2007) is ~ 40 times lower at low luminosities than that derived by Hao et al. (2005b) because of their more stringent sample selection criteria, but the two LFs are consistent with each other at the high-luminosity end ($L_{[\text{OIII}]} \sim 10^8 L_{\odot}$), that is, at luminosities relevant to our comparison.

3.4. How Many Type 2 Quasars have we Missed?

In principle, if we knew the distribution of optical SEDs and radio properties of type 2 quasars, we could calculate the probability with which each algorithm would select a type 2 quasar of a given $[\text{OIII}] 5008$ luminosity at every redshift. We could then use this information to correct the luminosity function for objects that are not in our sample because they do not have the optical colors, apparent magnitudes, optical morphologies, or radio fluxes that are targeted by the SDSS algorithms. The optical spectrum of a type 2 quasar is the sum of the host galaxy spectrum, the narrow lines and scattered light from the AGN (Zakamska et al. 2005, 2006). None of these components can be neglected, the relative strengths of the components vary from object to object, and even the shape of the host galaxy continuum matters for selection. For example, the Balmer break of the host galaxy moving across the r and i filters at redshift ~ 0.35 produces a difference in colors sufficient to enable or disable selection by the Low- z QSO algorithm in several objects. This selection effect results in the weak feature in the

[OIII]5008 luminosity-redshift distribution seen in upper right-hand panel of Fig. 5.

With the above complications in mind, we do not attempt to model the spectra of type 2 quasars. Instead, we derive quantitative estimates of the contributory power of the various target algorithms to the selection of type 2 quasars, directly from the data. We do not use these results to apply corrections to the LF, keeping with our ‘lower limit’ approach; but they are nonetheless useful in guiding the interpretation of the derived luminosity functions.

We define the contributory power of a given target algorithm to be the fraction of objects in the sample (871 objects with $L_{[\text{OIII}]} \geq 10^{8.1} L_{\odot}$) that we would select if we use this algorithm alone. We determine what this fraction would be if all objects were placed at a certain redshift (following §3.2). Figure 9 shows the resulting function for assumed redshifts in the range of 0.1 to 0.8 (in steps of 0.01) and for three ranges in [OIII]5008 luminosity. Not surprisingly, we find that the algorithms with deeper magnitude limits (Serendipity FIRST and High-z QSO) do better at selecting objects at high redshifts than the shallow ones (Galaxy and Low-z QSO). The color-based selection criteria of the Low-z QSO and High-z QSO cause the peaks and dips in their curves. We find that all four algorithms are poor at selecting low $L_{[\text{OIII}]}$ objects at high redshifts, which is why the derived type 2 quasar LF shows evidence for incompleteness there.

3.4.1. Contributory Power of Color-Based Target Algorithms

Another way to estimate the contributory power of the color-based target algorithms to the selection of type 2 quasars is to examine their overlap with the non-color based algorithms. Of the 258 Galaxy targets with redshifts $z < 0.2$, 254 (98%) are brighter than the magnitude limit of the Low-z QSO algorithm ($i_{\text{PSF}} = 19.1$) but only 12 of these (5%) have colors that satisfy the Low-z QSO selection criteria. Between $z = 0.2$ and 0.4, there are 137 Galaxy targets; 113 of them (82%) have $i_{\text{PSF}} \leq 19.1$, but only 1 object (0.9%) was selected by the Low-z QSO algorithm. The small amount of overlap between the Low-z QSO and Galaxy targets indicates that the Low-z QSO algorithm is missing many type 2 quasars because it is only

sensitive to a limited region of color space. There is no overlap at all between the High-z QSO and Galaxy algorithms. The colors of many type 2 quasars are dominated by the colors of their host galaxies, especially for lower [OIII] luminosities, and neither Low-z QSO nor High-z QSO algorithms target such objects.

Out of the 275 objects selected by the Serendipity FIRST target algorithm, 74 have $i_{\text{PSF}} \leq 19.1$ and 15 of these (20%) are targeted by the Low-z QSO algorithm; 245 have $i_{\text{PSF}} \leq 20.2$ and only 12 of these (5%) are targeted by the High-z QSO algorithm. These comparisons suggest that over the full redshift range, the Low-z QSO and High-z QSO algorithms select only 20% or less of type 2 quasars.

3.4.2. Low-redshift Objects and the Galaxy Target Algorithm

In this section, we discuss the interpretation of our LF calculation in the lowest redshift range, $z \leq 0.30$. We see from Fig. 5 that there are no objects in our sample with $L_{[\text{OIII}]} > 10^{9.5} L_{\odot}$ found at these redshifts, and only 1 out of 17 objects with $L_{[\text{OIII}]} > 10^{9.8} L_{\odot}$ is at $z \leq 0.5$. At face value, the scarcity of detected objects may be interpreted as a significant drop in the ratio of number densities of type 2 quasars at these luminosities. However, we argue here that this may instead be due to a combination of the selection effects and the small volume covered by the lowest redshift bin.

Most type 2 quasars in the redshift range 0.1 to 0.3 were selected by the Galaxy algorithm. The efficiency of the Galaxy algorithm begins to drop at redshifts around $z = 0.2$ due to its shallow magnitude limit (Figs. 5 and 9). Quantitatively, an object with $L([\text{OIII}]) = 10^{9.5} L_{\odot}$ at $z = 0.3$ with a rest-frame equivalent width of 500 \AA (corresponding to the median of the $L([\text{OIII}])/\text{EQW}[\text{OIII}]$ distribution for our sample; Paper I) would have an r band AB magnitude of around 17.8 mag, and would therefore not be selected by the Galaxy algorithm. As we discussed in the previous section, these objects may be missed by the color-based target algorithms because they do not lie in the specific regions of color-color space these algorithms were designed to target. The radio-based Serendipity FIRST algorithm would have a chance of picking out high-luminosity, low-redshift objects that happen to be radio-bright, but even the lu-

minous objects at low redshift may fall below the radio flux limits of the FIRST survey. More importantly, only $\sim 40\%$ of Serendipity FIRST targets have spectra (Section 3.2.4). Therefore, the fact that we have no type 2 quasars with $z \leq 0.30$ and $L[\text{OIII}] > 10^{9.5} L_{\odot}$ may be entirely due to the incompleteness of SDSS spectroscopic target selection.

4. Type 1 Quasar Luminosity Function

In order to put our type 2 quasar LF into context, we compare it with the type 1 LF which we calculate in this section using the same method as we have employed for type 2 quasars. We derive the $1/V_{\text{max}}$ [OIII]5007 LF from a complete sample of type 1 quasars using the formalism we have applied to the type 2 quasar sample (outlined in §3.1 above). We discuss the sample selection in §4.1, measurement of [OIII]5008 luminosities in §4.2, the calculation of the LF and results in §4.3, and in §4.4, we check that our derived LF agrees with previous work. The type 1 LF for the three redshift ranges is shown in Fig. 13.

4.1. Type 1 Quasar Sample

We select a complete sample of 8003 type 1 quasars from the SDSS DR5 Quasar Catalog (Schneider et al. 2007). The catalog consists of 77,429 spectroscopically-confirmed quasars in the redshift range 0.08-5.41, with absolute magnitude in the i band $M_i < -22$ mag and full width at half-maximum (FWHM) of lines from the broad-line region greater than 1000 km/s. From this catalog, 31,999 objects are targeted with the final version of the Low- z QSO algorithm (Richards et al. 2002). Of these, 8003 objects satisfy the redshift cut $z < 0.83$ and are included in our sample. The effective area of our sample is 4041 deg², calculated using the same procedure as in §3.1.

The redshift and [OIII]5008 luminosities of these objects are shown in the bottom-right panel of Fig. 5. There is no explicit lower cut in redshift, but there are very few objects with redshifts $z < 0.15$ because of the strong redshift evolution in the type 1 quasar population and the bright limit of the Low- z QSO target algorithm.

4.2. Measurement of [OIII]5008 Luminosities

In the calculation of the type 1 quasar LF, we use [OIII]5008 luminosities measured from Gaussian fits, after careful subtraction of FeII emission. The average contribution of FeII emission to the total flux over the wavelength range 5007 ± 1.7 FWHM is $\sim 9\%$. We exclude the region containing H β and [OIII]4959,5007 and find the best fit to the spectrum in the form of a power law plus the FeII template of Boroson & Green (1992). We then fit a set of four Gaussians to [OIII]4959, [OIII]5007, and narrow and broad components of H β . 5,297 quasars (67% of the sample) have $L_{[\text{OIII}]} > 10^{8.3} L_{\odot}$, and 221 quasars (2.8% of the sample) have $L_{[\text{OIII}]} > 10^{9.5} L_{\odot}$.

We also obtain a non-parametric line luminosity by integrating the detected flux density and subtracting the contribution from the continuum, FeII, H β , and [OIII]4959. For most objects, the Gaussian and integrated line fluxes are in good agreement. Outliers from the integrated vs. Gaussian locus were visually inspected, and 187 spectra (2.3% of the sample) for which the fit failed (due to low signal-to-noise ratio, bad pixels, etc.) were discarded.

4.3. $1/V_{\text{max}}$ Luminosity Function

Objects in the type 1 quasar sample were all selected by the Low- z QSO target algorithm, described in §3.2.2. In the case of type 2 quasars, we considered both the magnitude limits and color-based selection criteria. In contrast, type 1 quasar colors do not evolve strongly with redshift for $z < 2.2$ (Richards et al. 2001, 2002), so we do not expect the color-based selection criteria to be important in this case. For each object, we determine the available comoving volume V_{max} based only on the faint magnitude limit of the survey, $i_{\text{PSF}} = 19.1$, since the volume corresponding to the bright limit of the survey is negligibly small.

As in §3.2, we calculate scaled and k -corrected PSF magnitudes as a function of assumed redshift from the observed spectrum of each object. We determine z_{max} , the redshift at which the PSF magnitude reaches the limit of the survey. The available volume V_{max} is then given by

$$V_{\text{max}} = \frac{\Omega}{4\pi} \int_{z_1}^{\min(z_{\text{max}}, z_2)} \frac{dV_c}{dz}(z) dz, \quad (10)$$

where $\Omega = 4041 \text{ deg}^2$ is the effective survey area for this sample, z_1 and z_2 are the edges of the redshift range for which we are calculating the LF and $(dV_c/dz) dz$ is the comoving volume element in the redshift interval dz (e.g., Hogg 1999).

Figure 10 shows the volume-weighted [OIII]5008 luminosity function for type 1 quasars (calculated using Eqs. 5 and 6), for the same redshift ranges as for type 2 quasars. Our results reflect the positive redshift evolution of the type 1 quasar population (Schneider et al. 2007). The turn-over of the $0.50 < z \leq 0.83$ LF at low luminosities is an artifact due to the difficulty of measuring weak [OIII]5008 lines at these redshifts, since the line falls on the red end of the observed spectrum where the signal tends to be noisier. In §5, we compare these results with our derived type 2 quasar luminosity function to compare the space densities of the two populations.

4.4. Comparison with Richards et al. (2006) Broadband Type 1 Quasar Luminosity Function

In this section, we check whether our results are consistent with the type 1 quasar luminosity function derived by Richards et al. (2006) using quasars from the SDSS DR3 quasar catalog. As a measure of luminosity, they used the broadband absolute magnitude M_{2400} at around rest-frame wavelength 2400\AA , corresponding to the SDSS i band at $z = 2$ (e.g., Blanton et al. 2003). Figure 11 shows the relation between [OIII]5008 luminosity and broadband absolute magnitude M_{2400} in type 1 quasars. A strong correlation is detected; we find the mean relation

$$\log\left(\frac{L[\text{OIII}]}{L_\odot}\right) = -0.38M_{2400} - 0.62, \quad (11)$$

with an RMS scatter of 0.36 dex. In terms of luminosities, this relation is very close to linear (it has a slope of 0.95 in the $\log L_{2400}/\log L[\text{OIII}]$ plane). Following Marconi et al. (2004), we convolve the observed type 1 broadband LF (for $0.30 < z < 0.68$, from Table 6 of Richards et al. 2006) with a log normal probability distribution around Eq. 11 to derive a converted [OIII]5008 luminosity function.

Figure 12 shows that there is a good agreement between the converted [OIII]5008 LF and the [OIII]5008 LF for $0.30 < z \leq 0.50$ that we

have calculated in §4.3. The turn-over at the low $L_{[\text{OIII}]}$ end of the converted LF is due to the absolute magnitude cut-off, since there are no objects fainter than $M_{2400} \sim -23$ to scatter into these $L_{[\text{OIII}]}$ bins. The shape of the converted LF is sensitive to the assumed slope and scatter in the $L_{[\text{OIII}]}-M_{2400}$ relation. Figure 12 shows for comparison the converted [OIII]5008 luminosity function derived under assumption of a zero dispersion in the $L_{[\text{OIII}]}-M_{2400}$ relation (inconsistent with the observed LF).

5. Comparison of Type 1 and Type 2 Quasar Luminosity Functions

In this section, we use the type 1 and type 2 quasar luminosity functions derived above (shown together in Fig. 13) to obtain quantitative estimates of the type 2 quasar fraction (§5.1). We discuss what we can learn about the two populations in terms of their redshift evolution in §5.2 and their radio properties in §5.3.

5.1. Type 2 Quasar Fraction

Figure 13 shows that the type 1 and type 2 quasar luminosity functions are comparable in the regimes where we expect our type 2 quasar LF to be least affected by selection bias, the low-luminosity regime ($< 10^9 L_\odot$) for the redshift range $z \leq 0.30$ and the high-luminosity regime for redshift ranges $0.30 < z \leq 0.50$ and $0.50 < z \leq 0.83$.

The number density of quasars in a given luminosity range can be estimated by integrating the luminosity function over that range. We calculate the type 2 quasar fraction as the ratio of the type 2 to the total (type 1 + type 2) quasar number density. We have already described at the beginning of §3 why our derived type 2 LF is a lower limit. There are additional effects that make our calculation of the type 2 quasar fraction a lower limit: (i) the combination of selection effects and redshift evolution artificially lowers the type 2 quasar fraction that we derive (§5.2); (ii) there are indications that the [OIII]5008 line is slightly more extinguished in type 2 quasars than in type 1 quasars (§5.3); and (iii) we have assumed that the [OIII]5008 luminosity is independent of the obscured fraction and serves as a tracer of the bolometric luminosity. In practice, it is likely that the [OIII]5008

luminosity is higher for objects with a larger opening angle, since in this case more material is illuminated by the central source. As demonstrated by Krolik (1999), this dependence leads to a bias favoring unobscured objects in any [OIII]-flux selected sample.

Figure 14 shows our derived type 2 quasar fraction calculated in narrow bins in [OIII]5008 luminosity. In this Figure, we use our best lower bound to the type 2 quasar LF (including a correction for the probability of radio detection; see §3.2.4). For the $z \leq 0.30$ bin, we find that the type 2 quasar fraction is about 60% for $L_{[\text{OIII}]} = 10^{8.3}$ to $10^9 L_\odot$. For $z \leq 0.30$ and $0.30 < z \leq 0.50$, our strongest limits come from the highest luminosity bin, which constrain the type 2 quasar fraction to be at least 40% and 60% at $L_{[\text{OIII}]} \sim 5 \times 10^9 L_\odot$, respectively. For comparison, also shown are results from other studies (listed in the figure caption). At face value, our lower limits on the type 2 fraction are consistent with measurements from the X-ray surveys, but in practice the type 2 quasar fraction may be significantly higher than our lower limits, as discussed above.

5.2. Comparison of Redshift Evolution

In this section, we apply the V/V_{max} test (Schmidt 1968) to probe redshift evolution within the type 1 and type 2 samples. For a uniformly-selected, non-evolving population of objects, V/V_{max} is expected to be distributed uniformly between 0 and 1 and to have a mean value of 0.5. For an object with redshift within the range (z_1, z_2) , V/V_{max} is given by

$$\frac{V}{V_{\text{max}}} = \frac{\int_{z_1}^{z_{\text{obs}}} P_s(z) \frac{dV_c}{dz}(z) dz}{\int_{z_1}^{z_2} P_s(z) \frac{dV_c}{dz}(z) dz} \quad (12)$$

where z_{obs} is the observed redshift of the object and $(dV_c/dz)dz$ is the comoving volume element in the redshift interval dz . If there is positive redshift evolution within the redshift range, the mean values of V/V_{max} over the sample are greater than 0.5. Incompleteness in the sample can either mask or enhance this effect, by weighting the sample toward the lower or higher end of the redshift range.

In Table 3, we list the mean values of V/V_{max} calculated from the type 1 and type 2 quasar samples for the three redshift ranges we used previously. Our type 1 quasar sample is complete,

and the $\langle V/V_{\text{max}} \rangle$ values greater than 0.5 indicate the positive redshift evolution within the sample (Richards et al. 2006). On the other hand, our type 2 quasar sample is incomplete, so the deviation of $\langle V/V_{\text{max}} \rangle$ from 0.5 is due to a combination of redshift evolution and selection effects (see §3.4), which we do not attempt to disentangle. For two out of the three redshift ranges, $\langle V/V_{\text{max}} \rangle$ values are lower for the type 2 quasar sample than for the corresponding type 1 quasar sample.

Since our derived LFs are calculated for broad ranges in redshift, they are a weighted average of the true LFs over the redshifts within this range. The above results suggest that the type 1 quasar LFs are weighted toward the higher end of the redshift range, and therefore toward higher number densities, relative to the type 2 quasar LFs. Therefore, the combination of selection effects and redshift evolution of quasar number density artificially lowers the type 2 to type 1 ratio that we derive from these LFs.

5.3. Comparison of Radio Properties

In this section, we test whether the radio properties of type 2 quasars are statistically consistent with those of type 1 quasars. We test this hypothesis to the same limited extent that we have employed in §3.2.4 – that is, we test whether non-radio-selected type 2 and type 1 quasars have the same detection rate with FIRST within $2''$. We use a variation of the statistic defined in Eq. 8 for comparing two populations of objects:

$$u = \frac{(f_1 - f_2)^2}{\sqrt{f_1(1-f_1)f_2(1-f_2)}} \frac{N_1 N_2}{N_1 + N_2}. \quad (13)$$

Here N_1 and N_2 are the number of type 1 and type 2 quasars, respectively, in a given bin in the z - L [OIII] plane and f_1 and f_2 are the fractions of objects in this bin that are detected by FIRST. One difficulty is that type 1 and type 2 quasars are distributed very differently in the z - L [OIII] plane, so the bins have to be small enough that the probability of detection can be considered constant within each bin. The distribution of the statistic described by Eq. 13 (inspired by two-sample statistics from Peacock 1983) is not formally independent of f_i and N_i in the same sense that the distribution of Eq. 8 is independent of N and p (as shown in the Appendix). Using Monte-Carlo

simulations we found that the distribution of the value in Eq. 8 is very close to that of χ^2 with one degree of freedom, as long as f_1 and f_2 are not too close to 0 or 1 and as long as the number of objects in each bin is sufficiently large ($N_i \gtrsim 10$).

We find that the radio detection rates of the two populations are statistically indistinguishable for all except the low-redshift, low-luminosity objects. Type 2 quasars with $z < 0.25$, $8.0 < \log(L/L_\odot) < 8.5$ are significantly more likely to be detected in FIRST than type 1 quasars. One possibility is that the [OIII] emission line is systematically more extinguished by dust in type 2 quasars than in type 1 quasars. Correcting for 0.1 dex of this putative extinction removes the detection rate difference everywhere in the z - L [OIII] plane. We discuss this possibility further in §6.2.

6. Discussion

6.1. [OIII]5008 Luminosity as a Measure of Bolometric Luminosity

In this work, we use the [OIII]5008 line emission as a tracer of bolometric luminosity because we want to use a measure that is applicable to both obscured and unobscured AGN. This line arises from the narrow line region which extends outside the obscuring material thought to surround the broad-line region of type 2 AGN (Antonucci 1993; Urry & Padovani 1995). Observational support for this assumption comes from the similarity of IR/[OIII] ratios in type 1 and type 2 AGN found by Mulchaey (1994). Moreover, the [OIII]5008 line has the advantage of being strong and easily detected in most AGN, and Simpson (1998) and Kauffmann et al. (2003) have shown that it is a good tracer of AGN activity and is not severely contaminated by star formation.

For our type 1 quasar sample, [OIII]5008 luminosity correlates strongly with broadband luminosity at around 2400 Å (Fig. 11), as well as with the monochromatic continuum luminosity measured at rest-frame 5100 Å (linear correlation coefficient = 0.53). Moreover, we are able to recover the [OIII]5008 LF we have calculated from the observed broadband LF (Richards et al. 2006) (Fig. 12). Using our *Spitzer* observations of type 2 quasars, we will attempt to tie the [OIII]5008 luminosity to the IR luminosity in these objects and ultimately to their bolometric luminosity (Za-

kamska et al. 2008b). In the meanwhile, bolometric luminosities can be estimated by using, first, our $M_{2400} - L_{[\text{OIII}]}$ correlation and then the well-measured average type 1 quasar spectral energy distributions. For example, our highest [OIII] luminosity of $10^{10}L_\odot$ corresponds to the intrinsic UV luminosity of $M_{2400} = -28$ mag (Fig. 11). We use the average quasar SED from Vanden Berk et al. (2001) to calculate the corresponding luminosity in the B band, and then using the bolometric corrections by Marconi et al. (2004), we estimate that the corresponding bolometric luminosity is 4×10^{47} erg/sec.

6.2. Reddening and Extinction

We expect some amount of extinction in the [OIII]5008 line, e.g., due to dust within the host galaxy. In this work, we have used line luminosities that are not corrected for this reddening. This means that heavily-reddened objects are not included in our sample. Moreover, in our calculation of the luminosity function, objects with [OIII] affected by extinction have been assigned to lower luminosity bins; this means that the luminosity function would be shifted toward the right (i.e., higher luminosities) if extinction-corrected luminosities were used. Without knowing the distribution of extinctions, it is hard to quantify the effect of this correction on the derived space density of type 2 quasars.

For the calculation of type 2 fraction it is the relative extinction in the [OIII]5008 line in type 1 and type 2 quasars that matters. In the optical, a direct comparison of extinction is difficult, since the estimates of extinction from the Balmer decrement (the ratio of the $H\alpha$ and $H\beta$ fluxes) are sensitive to obscuration from different physical regions. For type 1 quasars, one measures the broad-line Balmer decrement which is sensitive to obscuration in the sub-parsec sized broad-line region (it is very difficult to isolate the narrow component of the lines, so what is usually measured is the sum of the narrow and broad components, which is dominated by the latter). For type 2 quasars, one measures the narrow-line Balmer decrement, which is sensitive to the outer narrow-line region, hundreds of parsecs to kilo-parsecs in size. Furthermore, Balmer decrements cannot be measured from SDSS spectra for objects with redshifts beyond 0.35, since the $H\alpha$ line falls outside the ob-

served spectral range at these redshifts. Finally, if a significant fraction of narrow line emission is produced inside the optically thick obscuring material, this portion of the emission would not be seen in type 2 quasars, and the line would be dimmed without any effect on the Balmer decrement. Therefore, small Balmer decrements do not necessarily imply small extinction.

With these caveats in mind, we searched the literature for calculations of the extinction in type 1 and type 2 AGN. Seyfert 1 galaxies have typical broad-line Balmer decrements of 3.5 (Adams et al. 1975; Osterbrock 1977), which, taken at face value, correspond to an [OIII]5008 line attenuation of about 0.65 mag, assuming an intrinsic Balmer decrement of 2.85 and the standard SMC reddening curve (Osterbrock 1989, Hopkins et al. 2004). For Seyfert 2 galaxies, Dahari & De Robertis (1988) measured narrow-line Balmer decrements of 64 objects and found a mean [OIII]5008 attenuation of ~ 2.5 mag. More recently, Kauffmann et al. (2003) studied type 2 AGN in DR1 and found [OIII]5008 attenuation up to ~ 2.5 -3 mag for [OIII]5008 luminosities close to $10^{8.3}L_{\odot}$. For our sample of type 2 quasars, we find a median attenuation of 1.5 mag from the measured Balmer decrements where they are available. These values suggest that the [OIII]5008 line is more attenuated in type 2 than type 1 quasars; we have found some evidence for a similar trend from the comparison of their radio properties (see §3.2.4). Additionally, IR observations strongly suggest that the narrow line regions of type 2 quasars are significantly more obscured than those of type 1 quasars, by up to a factor of 10 (Haas et al. 2005). This is one of the reasons why the type 2 quasar fraction we derive is a lower bound of the true value.

6.3. Implications for the Black Hole Mass Function and Accretion Efficiency

If black holes grow primarily by accretion, the total luminosity emitted by accretion processes over the lifetime of the Universe is directly related to the accumulated mass of local supermassive black holes (Soltan 1982; Yu & Tremaine 2002). Recent measurements of both the mass density of supermassive black holes and the total luminosity emitted by matter accreted onto them can be reconciled if the radiative efficiency (the fraction of the accreted mass that is converted directly into

observed quasar radiation) is quite high, $\epsilon \gtrsim 0.1$ (Yu & Tremaine 2002; Marconi et al. 2004; Barger et al. 2005). In this section we discuss qualitatively how these calculations are affected by the existence of a large population of obscured quasars.

What matters for quantifying the growth of the black hole is its total energetic output ('bolometric luminosity' L_{bol}), since that is the value that can be related to the accreted mass through radiative efficiency. Some of the optical, UV and X-ray radiation is intercepted by the obscuring material and then re-emitted in the IR more or less isotropically, but no new energy is generated. The ratio of energy reprocessed this way roughly equals $f(L_{bol})L_{bol}$, where $f(L_{bol})$ is the fraction of obscured AGN in the population and $4\pi f(L_{bol})$ is the solid angle covered by obscuring material as seen from the central engine. Since the IR emission is directly related to the obscuration fraction, it is possible to derive the obscured fraction from the IR-to-optical ratio in unobscured quasars (Treister et al. 2007).

Some of the accretion efficiency calculations are based on the optical LF of type 1 quasars (e.g., Yu & Tremaine 2002). In this case, the luminosity of each individual quasar is overestimated by including the IR emission in the bolometric correction, but the total number of objects is underestimated. The net result is that the contribution of quasars with bolometric luminosities L_{bol} to the luminosity budget should be augmented by roughly $1/(1 - f^2(L_{bol}))$ to account for the obscured sources. Other recent calculations are based on the hard X-ray luminosity functions of AGN (Marconi et al. 2004; Barger et al. 2005) in an effort to include both obscured and unobscured AGN, but this procedure misses the contribution from Compton-thick sources. The most recent accretion efficiency estimates are based on combining optical and X-ray data to produce bolometric luminosity functions (Hopkins et al. 2007; Shankar et al. 2007). Nevertheless, the fraction of Compton-thick sources which would be missed by both X-ray surveys and type I AGN surveys remains a major uncertainty in these methods. If $f_C(L_{bol})$ is the Compton-thick fraction of type 2 AGN, then the contribution of AGN with bolometric luminosities L_{bol} should be increased by $1/(1 - f_C(L_{bol})f(L_{bol}))$. Assuming $f_C \gtrsim 0.5$ (Risaliti 1999) and $f \gtrsim 0.5$ (this work) for quasars

around and above the luminosity function break, we find that both types of methods (those based on the optically selected AGN and those based on X-ray selected AGN) may underestimate the AGN luminosity budget by 30% or more. This means that the calculated accretion efficiency would be underestimated by the same amount.

7. Summary and Conclusions

In this paper, we present 887 optically-selected type 2 quasars with redshifts $0 < z \lesssim 0.83$ (Table 1), which is the largest sample of type 2 quasars to date. These objects are selected from the spectroscopic database of the SDSS on the basis of their emission line properties. Candidate sources are required to have no broad (FWHM > 1100 km/sec) components in their permitted emission lines. To distinguish type 2 AGN from star-forming galaxies, we use the standard line diagnostic diagrams involving [OIII]/H β , [NII]/H α and [SII]/H α line ratios (at redshifts $z < 0.3$) or require other signs of a hidden AGN, such as the presence of the [NeV]3347,3427 emission lines (at redshifts $0.3 < z < 0.8$). We place a lower limit on the [OIII]5008 line luminosity of $10^{8.3} L_{\odot}$, ensuring that the bolometric luminosities of these objects are above the classical Seyfert/quasar separation of 10^{45} erg/sec.

For this sample, we calculate the [OIII] luminosity function using the $1/V_{\max}$ method (Fig. 8). The selection function that we calculate for each object involves taking into account four different spectroscopic target selection algorithms, of which two (Low- z QSO and High- z QSO) are color-based, one (Main Galaxy) is based on optical morphology and one (Serendipity FIRST) is based on the radio properties. By comparing how well each algorithm performs at selecting type 2 quasars, we find that color-based algorithms are rather ineffective and select no more than 20% of objects. Indeed, there is no well-defined region of the color-color space where type 2 quasars concentrate, even when only narrow redshift ranges are considered. The success of the SDSS in selecting a large number of type 2 quasars is due to the unprecedented size of the spectroscopic survey and the multitude of different target selection algorithms which allow for serendipitous objects.

We extend the [OIII]5008 AGN luminosity

function to luminosities about 2 orders of magnitude higher than was previously done, up to $L_{[\text{OIII}]} \simeq 10^{10} L_{\odot}$. This value corresponds to the intrinsic UV luminosity of $M_{2400} = -28$ mag and the bolometric luminosity of 4×10^{47} erg/sec.

We also derive the [OIII] luminosity function for a complete sample of 8003 $z < 0.83$ type 1 quasars taken from the SDSS quasar catalog and find it to be in excellent agreement with other measurements. We can then directly compare the luminosity functions of type 1 and type 2 quasars (Fig. 13) and constrain the type 2 quasar fraction as a function of luminosity (Fig. 14). We argue that the type 2 quasar luminosity function and the type 2 quasar fraction that we derive are strong lower limits. The main reasons are that (i) there may be a significant number of type 2 quasars that do not meet our spectroscopic selection criteria, and (ii) narrow lines are more extinguished in type 2 quasars than they are in type 1 quasars, biasing the type 2/type 1 ratio at a given luminosity to lower values.

Objects with different [OIII] luminosities and different redshifts suffer from different selection biases. Our best data are at low redshifts and relatively low luminosities ($z < 0.3$ and $L_{[\text{OIII}]} < 10^9 L_{\odot}$) and at high redshifts and relatively high luminosities ($0.50 < z \leq 0.83$ and $L_{[\text{OIII}]} > 10^{9.5} L_{\odot}$). In these regimes we find that type 2 quasars are more abundant than type 1 quasars, with the type 2/type 1 ratios of 1.5:1 and 1.2:1, correspondingly.

Acknowledgments

NLZ is supported by the NASA Spitzer Space Telescope Fellowship Program through a contract issued by the Jet Propulsion Laboratory, California Institute of Technology under a contract with NASA. RR and MAS are supported by NSF grant AST-0707266. Support for this work was also provided by the NASA through Chandra X-ray Observatory Center, which is operated by the Smithsonian Astrophysical Observatory for and on behalf of the NASA under contract NAS8-03060.

Funding for the SDSS and SDSS-II has been provided by the Alfred P. Sloan Foundation, the Participating Institutions, the National Science Foundation, the U.S. Department of Energy, the National Aeronautics and Space Administration,

the Japanese Monbukagakusho, the Max Planck Society, and the Higher Education Funding Council for England. The SDSS is managed by the Astrophysical Research Consortium for the Participating Institutions. The Participating Institutions are the American Museum of Natural History, Astrophysical Institute Potsdam, University of Basel, Cambridge University, Case Western Reserve University, University of Chicago, Drexel University, Fermilab, the Institute for Advanced Study, the Japan Participation Group, Johns Hopkins University, the Joint Institute for Nuclear Astrophysics, the Kavli Institute for Particle Astrophysics and Cosmology, the Korean Scientist Group, the Chinese Academy of Sciences (LAMOST), Los Alamos National Laboratory, the Max-Planck-Institute for Astronomy (MPIA), the Max-Planck-Institute for Astrophysics (MPA), New Mexico State University, Ohio State University, University of Pittsburgh, University of Portsmouth, Princeton University, the United States Naval Observatory, and the University of Washington.

Appendix

In this appendix, we prove our assertion in §3.2.4 that the statistic u , defined by Eq. 8, follows a χ^2 distribution with one degree of freedom. We have N quasars with the same redshift and [OIII] luminosity, of which n are detected in the radio, so the measured detection rate is $f = n/N$. We would like to test the null hypothesis (NH) that the underlying probability of detection (for this redshift and luminosity) is p (denoted as $p_{\text{RD}}(z, L_{\text{[OIII]}})$ in the text). If it were indeed p , then the probability of detecting n objects out of N would be binomial:

$$R(n) = C_N^n p^n (1-p)^{N-n}. \quad (14)$$

For very large N ($\sqrt{Np} \gg 1$), this distribution is close to a Gaussian

$$r(n)dn = \frac{1}{\sqrt{2\pi\sigma^2}} e^{-\frac{(n-pN)^2}{2\sigma^2}} dn, \quad (15)$$

where $\sigma^2 = Np(1-p)$. We now define a function of the observed values n and N and the underlying probability p :

$$u(n) = \frac{(n-pN)^2}{Np(1-p)}. \quad (16)$$

The probability density of u , i.e., the probability to find this variable in the range between u and $u + du$ under the assumption of the NH is

$$r_u(u)du = \frac{2r(n)}{|du/dn|} du = \frac{1}{\sqrt{2\pi u}} e^{-u/2} du \quad (17)$$

for $u > 0$, and $r_u(u) = 0$ otherwise. In other words, the distribution of u does not depend on N or p for large values of N . The distribution function (17) is that of χ^2 with one degree of freedom. Given a measurement n and N , if we want to test whether it is consistent with the underlying probability p , we calculate u . If $u > 6.5$, then the NH is ruled out with a 99% probability.

REFERENCES

- Abazajian, K., et al. 2003, AJ, 126,2081 (DR1 paper)
- Abazajian, K., et al. 2004, AJ, 128, 502 (DR2 paper)
- Adams, T. F., & Weedman, D. W. 1975, ApJ, 199, 19
- Adelman-McCarthy, J., et al. 2006, ApJS, 162, 1 (DR4 paper)
- Adelman-McCarthy, J., et al. 2007a, ApJS, 172, 634 (DR5 paper)
- Adelman-McCarthy, J., et al. 2007b, ApJS, in press (arXiv:0707.3413; DR6 paper)
- Anderson, A. et al. 2007, AJ, 133, 313
- Antonucci, R. 1993, ARA&A, 31, 473
- Baldwin, J. A., Phillips, M. M., & Terlevich, R. 1981, PASP, 93, 5
- Barger, A. J., Cowie, L. L., Mushotzky, R. F., Yang, Y., Wang, W.-H., Steffen, A. T., Capak, P. 2005, AJ, 129, 578
- Becker, R. H., White, R. L., & Helfand, D. J. 1995, ApJ, 450, 559
- Beckmann, V., Soldi, S., Schrader, C. R., Gehrels, N., & Produit, N. 2006, ApJ, 652, 126
- Blanton, M. R., Lupton, R. H., Maley, F. M., Young, N., Zehavi, I., & Loveday, J. 2003, AJ, 125, 2276

- Boroson, T. A. & Green, R. F. 1992, *ApJS*, 80, 109
- Brand, K. et al. 2007, *ApJ*, 663, 204
- Brusa, M. et al. 2007, *ApJS*, 172, 353
- Comastri, A., Setti, G., Zamorani, G. & Hasinger, G. 1995, *A&A*, 296, 1
- Dahari, O., & De Robertis, M. M., 1988, *ApJ*, 331, 727
- Djorgovski, S. G., et al. 2001, *ASP Conf. Ser.* 225, *Virtual Observatories of the Future*, ed. R. Brunner, S. G. Djorgovski, & A. Szalay (San Francisco: ASP), 52
- Eisenstein, D.J., et al. 2001, *AJ*, 122, 2267
- Fukugita, M., Ichikawa, T., Gunn, J. E., Doi, M., Shimasaku, K., & Schneider, D. P. 1996, *AJ*, 111, 1748
- Gilli, R., Comastri, A., & Hasinger, R. 2007, *A&A*, 463, 79
- Greene, J. & Ho, L. 2007, *ApJ*, 667, 131
- Groves, B., Dopita, M. & Sutherland, R. 2004, *ApJS*, 153, 75
- Gunn, J. E., et al. 1998, *AJ*, 116, 3040
- Gunn, J. E., et al. 2006, *AJ*, 131, 2332
- Haas, M., Siebenmorgen, R., Schulz, B., Krugel, E., and Chini, R. 2005, *A&A*, 442, 39
- Hao, L., et al. 2005a, *AJ*, 129, 1783
- Hao, L., et al. 2005b, *AJ*, 129, 1795
- Heckman, T. M., van Breugel, W. J. M., & Butcher, H. R. 1981, *ApJ*, 247, 403
- Heckman, T. M., et al. 2005, *ApJ*, 634, 161
- Hogg, D.W. 1999, preprint (astro-ph/9905116)
- Hogg, D. W., Schlegel, D. J., Finkbeiner, D. P., & Gunn, J. E. 2001, *AJ*, 122, 2129
- Hogg, D. W., Baldry, I. K., Blanton, M. R. & Eisenstein, D. J. 2002, preprint (astro-ph/0210394)
- Hopkins, P. F., et al. 2004, *AJ*, 128, 1112
- Hopkins, P. F., Hernquist, L., Cox, T. J., Di Matteo, T., Robertson, B., & Springel, V. 2006, *ApJS*, 163, 1
- Hopkins, P. F., Richards, G. T., & Hernquist, L. 2007, *ApJ*, 654, 731
- Huchra, J. & Burg, R. 1992, *ApJ*, 393, 90
- Ivezić, Ž., et al. 2004, *Astron. Nachr.*, 325, 583
- Kauffmann, G., et al. 2003, *MNRAS*, 346, 1055
- Keel, W.C., de Grijp, M.H.K., Miley, G.K., & Zheng, W. 1994, *A&A*, 283, 791
- Kewley, L. J., Dopita, M. A., Sutherland, R. S., Heisler, C. A., & Trevena, J. 2001, *ApJ*, 556, 121
- Kleinmann, S. G., Hamilton, D., Keel, W. C., Wynn-Williams, C. G., Eales, S. A., Becklin, E. E., & Kuntz, K. D. 1988, *ApJ*, 328, 161
- Krolik, J.H. 1999, *Active Galactic Nuclei: From the Central Black Hole to the Galactic Environment* (Princeton: Princeton University Press) [pp. 456-459 for biases in the line-selected samples]
- Lacy, M., Canalizo, G., Rawlings, S., Sajina, A., Storrie-Lombardi, L., Armus, L., Marleau, F. R., Muzzin, A. 2005, *Memorie della Societa Astronomica Italiana*, 76, 154
- Lacy, M., Petric, A. O., Sajina, A., Canalizo, G., Storrie-Lombardi, L. J., Armus, L., Fadda, D., Marleau, F. R. 2007, *AJ*, 133, 186
- Lacy, M., et al. 2004, *ApJS*, 154, 166
- Lawrence, A. 1991, *MNRAS*, 252, 586
- Lupton, R.H., Gunn, J.E., & Szalay, A.S. 1999, *AJ*, 118, 1406
- Marconi, A., Risaliti, G., Gilli, R., Hunt, L.K., Maiolino, R. & Salvati, M. 2004, *MNRAS*, 351, 169
- Markwardt, C. B., Tueller, J., Skinner, G. K., Gehrels, N., Barthelmy, S. D., Mushotzky, R. F. 2005, *ApJ*, 633, 77
- Martínez-Sansigre, A., et al. 2006, *MNRAS*, 370, 1479

- Martínez-Sansigre, A., et al. 2007, MNRAS, 379, L6
- Mulchaey, J.S., Koratkar, A., Ward, M.J., Wilson, A.S., Whittle, M., Antonucci, R. R. J., Kinney, A. L., Hurt, T. 1994, ApJ, 436, 586
- Nagao, T., Maolino, R. & Marconi, A. 2006, A&A, 447, 863
- Norman, C., et al. 2002, ApJ, 571, 218
- Osterbrock, D. E. 1977, ApJ, 215, 733
- Osterbrock, D. E. 1989, *Astrophysics of Gaseous Nebulae and Active Galactic Nuclei* (Mill Valley CA: University Science Books)
- Osterbrock, D. E. & Shaw, R. A. 1988 ApJ, 327, 89
- Padmanabhan, N., et al. 2007, ApJ, in press, astro-ph/0703454
- Peacock, J.A. 1983, MNRAS, 202, 615
- Petrosian, V. 1976, ApJ, 210, L53
- Pier, J. R., Munn, J. A., Hindsley, R. B., Hennessy, G. S., Kent, S. M., Lupton, R. H., & Ivezić, Ž. 2003, AJ, 125, 1559
- Polletta, M. 2006, ApJ, 642, 673
- Polletta, M., Weedman, D., Hoenig, S., Lonsdale, C. J., Smith, H. E., Houck, J. 2007, arxiv:0709.4458
- Ptak, A., Zakamska, N. L., Strauss, M. A., Krolik, J. H., Heckman, T. M., Schneider, D. P., & Brinkmann, J., ApJ, 637, 147
- Richards, G. T., et al. 2001, AJ, 21, 2308
- Richards, G. T., et al. 2002, AJ, 123, 2945
- Richards, G.T., et al. 2006, AJ, 131, 2766
- Rigby, J. R., Rieke, G. H., Donley, J. L., Alonso-Herrero, A. & Pérez-González, P. G. 2006, ApJ, 645, 115
- Risaliti, G., Maiolino, R., & Salvati, M. 1999, ApJ, 522, 157
- Salzer, J. 1989, ApJ, 347, 152
- Sandage, A. 1961, ApJ, 133, 335
- Sazonov, S., Revnivtsev, M., Krivonos, R., Churazov, E., Sunyaev, R. 2007, A&A, 462, 57
- Schlegel, D. J., Finkbeiner, D. P., & Davis, M. 1998, ApJ, 500, 525
- Schmidt, M. 1968, ApJ, 151, 393
- Schneider, D. P., et. al. 2007, AJ, 134, 102
- Shankar, F., Weinberg, D. H., & Miralda-Escudé, J. 2007, ApJ, submitted (arxiv:0710.4488)
- Shen, Y., et al. 2007, AJ, 133, 2222
- Simpson, C. 1998, MNRAS, 297, L39
- Simpson, C. 2005, MNRAS, 360, 565
- Smith, J. A., et al. 2002, AJ, 123, 2121
- Soltan, A. 1982, MNRAS, 200, 115
- Stern, D., et al. 2002, ApJ, 568, 71
- Stern, D., et al. 2005, ApJ, 631, 163
- Stoughton, C., et al. 2002, AJ, 123, 485
- Strauss, M. A., et al. 2002, AJ, 124, 1810
- Sturm, E., et al. 2006, ApJ, 642, 81
- Subbarao, M., Frieman, J., Bernardi, M., Loveday, J., Nichol, B., Castander, F., & Meiksin, A. 2002, SPIE, 4847, 452
- Szokoly, G. P., et al. 2004, ApJS, 155, 271
- Tucker, D. L., et al. 2006, Astron. Nachr. 327, 821
- Treister, E., Urry, C. M. & Lira, P. 2006, *Revista Mexicana de Astronomia y Astrofisica*, 26, 147
- Treister, E., Krolik, J., & Dullemond, C. 2007, ApJ, submitted
- Ueda, Y., Akiyama, M., Ohta, K., Miyaji, T. 2003, ApJ, 598, 886
- Vanden Berk, D.E., et al. 2001, AJ, 122, 549
- Veilleux, S., & Osterbrock, D. E. 1987, ApJS, 63, 295
- Vignali, C., Alexander, D., & Comastri, A. 2004, MNRAS, 354, 720

Vignali, C., Alexander, D., & Comastri, A. 2006, MNRAS, 373, 321

Voges, W., et al. 1999, A&A, 349, 389

Urry, C. M. & Padovani, P. 1995, PASP, 107, 803

Whittle, M. 1985, MNRAS, 216, 817

York, D. G., et al. 2000, AJ, 120, 1579

Yu, Q. & Tremaine, S. 2002, MNRAS, 335, 965

Zakamska, N. L., et al. 2003, AJ, 126, 2125 (Paper I)

Zakamska, N. L., Strauss, M.A., Heckman, T.M., Ivezić, Ž., & Krolik, J.H. 2004, AJ, 128, 1002

Zakamska, N. L., et al. 2005, AJ, 129, 1212

Zakamska, N. L., et al. 2006, AJ, 637, 147

Zakamska, N. L., et al. 2008a, in preparation

Zakamska, N. L., et al. 2008b, in preparation

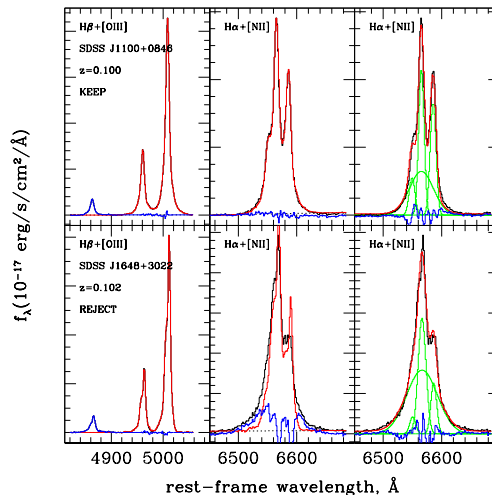


Fig. 1.— Examples of our non-parametric fitting procedure to determine whether there is a broad component in $H\alpha$ line. From left to right, the three panels for each object are: (i) the $H\beta$ + $[OIII]$ complex and model fits to the blue wing of $[OIII]4960$ and the red wing of $[OIII]5008$; (ii) fit of the $H\alpha$ + $[NII]$ complex, using the $[OIII]4960, 5008$ line profile for all three lines; (iii) the best 4-Gaussian fit to the $H\alpha$ + $[NII]$ complex. In each panel, the original spectrum is in black, the model is in red, residuals are in blue and the four Gaussian components are in green. Although for both objects the 4-Gaussian fit to the $H\alpha$ + $[NII]$ complex is statistically preferred to the 3-Gaussian fit, in SDSS J1100+0846 (upper panel) this complex is well-fit with a blend of lines shaped like $[OIII]$, so we keep this object in our sample. In SDSS J1648+3022 (lower panel), the complex is significantly broader than the blend of $[OIII]$ lines, as indicated by the fit residuals, so we classify this object as a broad-line AGN and exclude it from our sample.

This 2-column preprint was prepared with the AAS L^AT_EX macros v5.2.

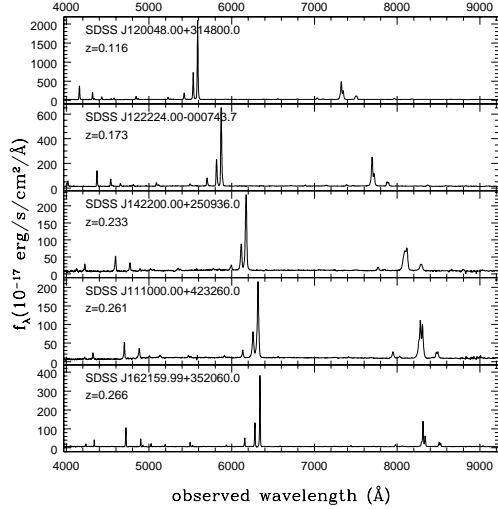


Fig. 2.— Example spectra of the highest luminosity type 2 quasars in the redshift range $z \leq 0.30$, smoothed by 5 pixels for display purposes. Objects in this plot have $L_{[\text{OIII}]5008} > 1.8 \times 10^9 L_{\odot}$. The strongest emission line is [OIII]5008.

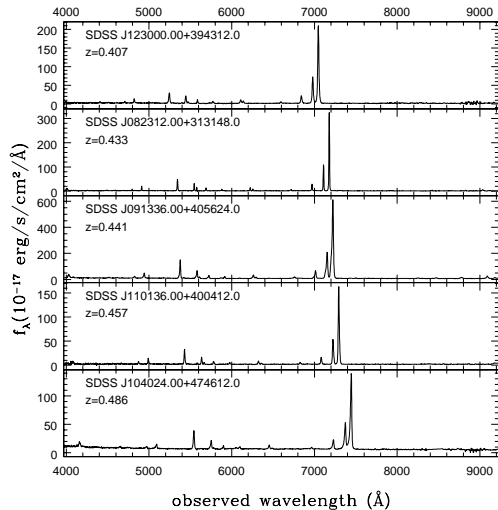


Fig. 3.— Same as Fig. 2, but for the redshift range $0.30 < z \leq 0.50$. These objects have $L_{[\text{OIII}]5008} > 5 \times 10^9 L_{\odot}$.

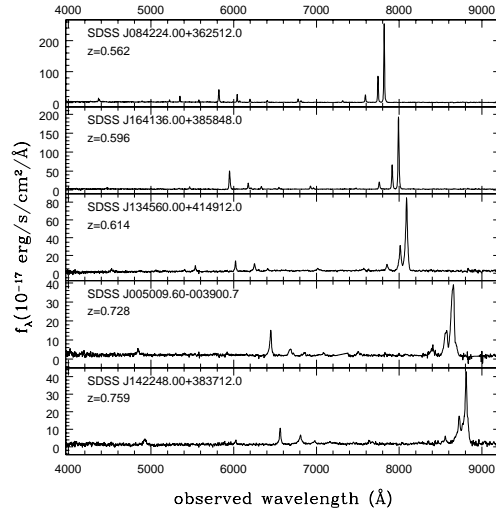


Fig. 4.— Same as Fig. 2, but for the redshift range $0.50 < z \leq 0.83$. These objects have $L_{[\text{OIII}]5008} > 9.6 \times 10^9 L_{\odot}$.

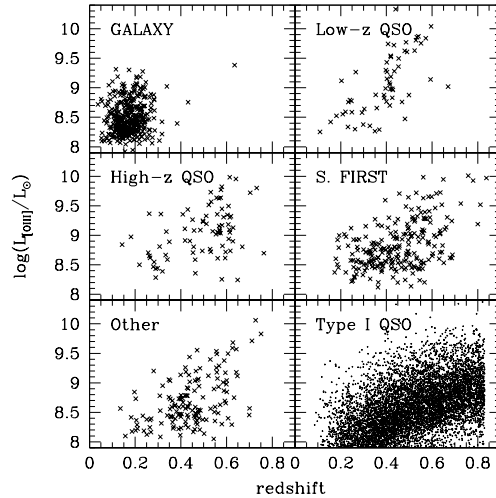


Fig. 5.— Distribution of [OIII]5008 luminosities and redshifts of type 2 quasars targeted by the Galaxy (366 objects), Low- z QSO (76), High- z QSO (89), Serendipity FIRST (276), and other (147) target algorithms. Some objects are targeted by multiple algorithms and thus appear in multiple panels in this Figure. Also shown is the distribution for type 1 quasars (8003 objects; see §4.1).

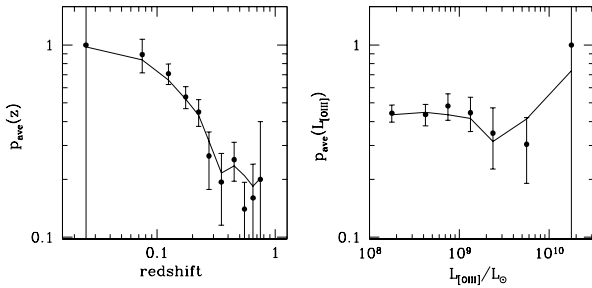


Fig. 6.— Comparison of the observed probability of FIRST detections with the best-fitting function for $p_{RD}(z, L_{[OIII]})$ (Eq. 9) for non-radio-selected type 2 quasars. Left: in each redshift range $z_1 \leq z < z_2$, the circle shows the value n/N , where n is the number of radio detected objects in this bin and N is the total number of objects. The Poisson error bars reflect the total number of objects contributing to each bin. The solid line connects values $p_{ave}(z) = \sum_i p_{RD}(z_i, L_i)/N$, where the summation is over all objects in this bin. Right: same, but for luminosity bins instead of redshift bins. Such representation allows us to properly take into account the distribution of objects in the z - $L_{[OIII]}$ plane.

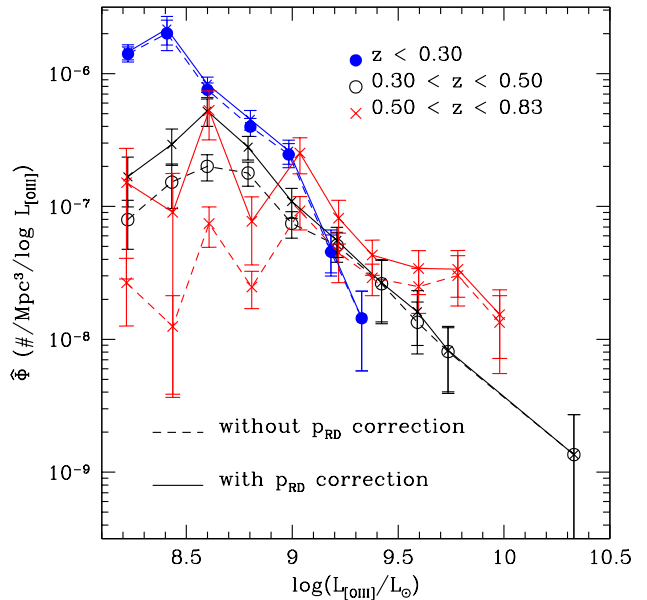


Fig. 7.— Volume-weighted [OIII]5008 luminosity function of type 2 quasars (lower limits) for three redshift ranges, with and without correction for the probability of radio detection (see §3.2.4; solid and dashed curves, respectively). The maximum volume is calculated using the selection criteria of the various SDSS spectroscopic target selection algorithms (see §3.2). Included in the calculation are 871 objects targeted by the top four Main survey algorithms (Galaxy, Low- z QSO, High- z QSO, and Serendipity FIRST).

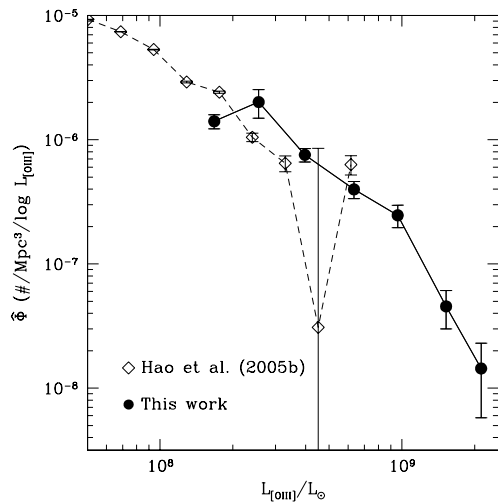


Fig. 8.— [OIII]5008 luminosity function of type 2 quasars (same as blue solid curve in Fig. 7) for $z \leq 0.30$, compared with that derived by Hao et al. (2005b). We find good agreement between the two functions in luminosity range in which they overlap. Here, the luminosities from Hao et al. (2005b) had been shifted by 0.14 dex to account for the difference in their spectrophotometric flux calibration scale (see §2.3).

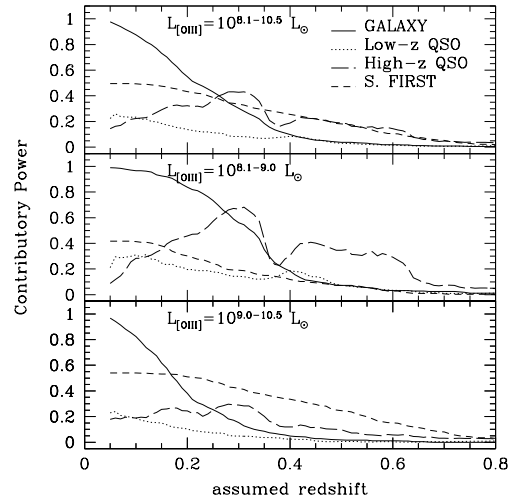


Fig. 9.— Contributory power of the various SDSS target algorithms (as labeled)— the fraction of objects in the type 2 quasar sample that would be selected by the algorithm taken alone. We place objects at different redshifts (in steps of $\Delta z = 0.01$) to determine this quantity as a function of assumed redshift. The three panels show the results for different ranges in [OIII]5008 luminosity. All four algorithms are poor at selecting low $L_{[\text{OIII}]}$ objects at high redshifts, which is why the derived type 2 quasar LF shows evidence for incompleteness there.

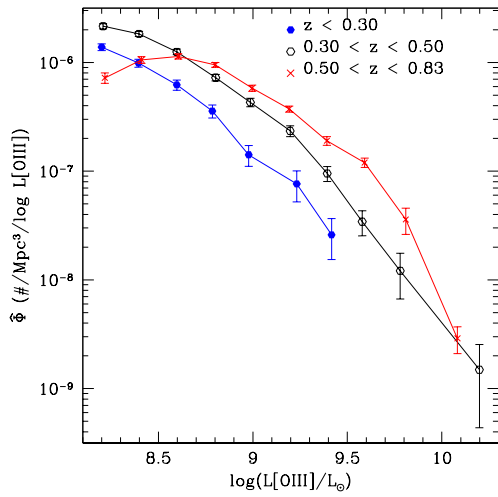


Fig. 10.— Volume-weighted [OIII]5008 luminosity function of type 1 quasars for three ranges in redshift. The maximum volume is calculated using the magnitude limit of the Low- z QSO target algorithm. The turn-over of the $0.50 < z \leq 0.83$ LF at low luminosities is an artifact due to the difficulty of measuring weak [OIII]5008 lines at these high redshifts.

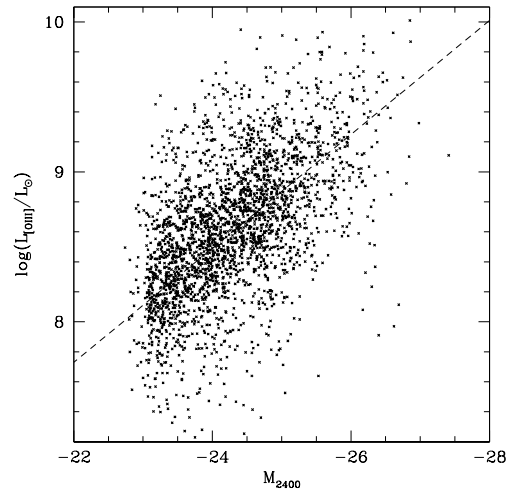


Fig. 11.— Correlation between broadband absolute magnitude M_{2400} and [OIII]5008 luminosity for type 1 quasars (used by Richards et al. 2006). We find the mean relation to be $\log(L[\text{OIII}]/L_{\odot}) = -0.38M_{2400} - 0.62$ (dashed line), with an RMS scatter of 0.36 dex. In terms of luminosities, the slope of this relation is 0.95. Here, M_{2400} is measured at around rest-frame wavelength 2400 Å, corresponding to the SDSS i band k -corrected to $z = 2$.

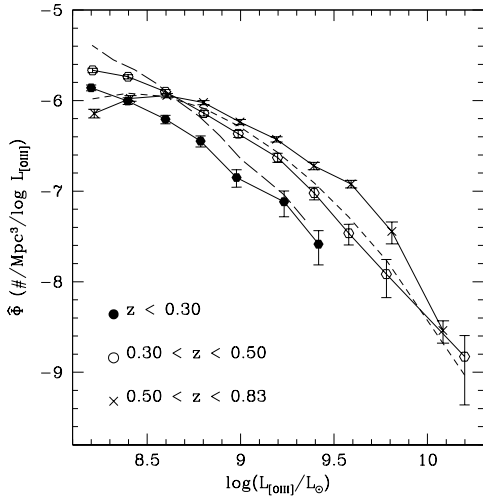


Fig. 12.— Comparison of the derived [OIII]5008 luminosity function of type 1 quasars with previous work. We convolve the broadband LF derived by Richards et al. (2006) for $0.30 < z < 0.68$ with the mean $L_{[OIII]}-M_{2400}$ relation given by Eq. 11 with a 0.36 dex scatter. The converted [OIII]5008 luminosity function (short-dashed curve) is in good agreement with the derived LF in the redshift range $0.30 < z \leq 0.50$. The shape of the converted LF is sensitive to the assumed scatter in the $L_{[OIII]}-M_{2400}$ relation. Also shown is the converted [OIII]5008 LF derived under the assumption of zero scatter (long-dashed curve), which is inconsistent with the derived LF.

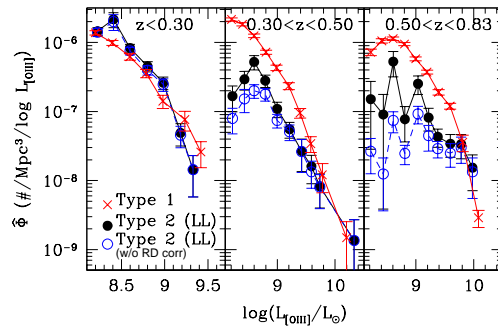


Fig. 13.— Comparison of the [OIII]5008 luminosity functions of type 1 and type 2 quasars, for three ranges in redshift. The type 2 quasar luminosity function (**lower limits**) with and without the correction for the probability of radio-detection (see §3.2.4) are shown (black solid and blue open circles, respectively). The type 2 quasar sample suffers from incompleteness, especially at low [OIII]5008 luminosities and high redshifts, as discussed above. Nevertheless, we find that the derived space densities of type 1 and type 2 quasars are comparable for the redshift range $z \leq 0.30$ and for the highest luminosities for the higher redshifts $0.3 < z \leq 0.83$.

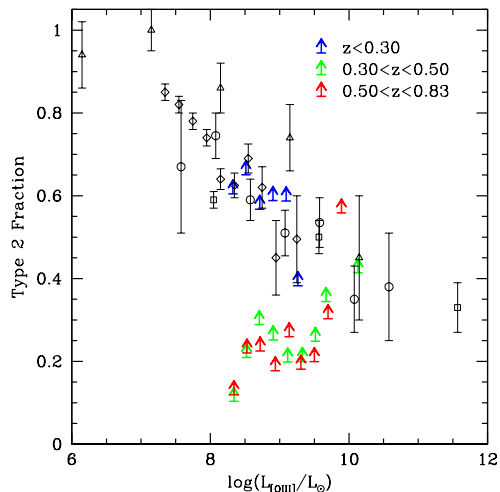


Fig. 14.— Lower limits to the type 2 quasar fraction— the ratio of type 2-to-total (type 1 + type 2) quasar number densities— for three ranges in redshift: $z \leq 0.30$ (blue), $0.30 < z \leq 0.50$ (green) and $0.50 < z \leq 0.83$ (red). Number densities are estimated by integrating the luminosity function over bins in [OIII]5008 luminosity. In this Figure, we use our best lower bound to the type 2 quasar LF (including a correction for the probability of radio detection; see §3.2.4). For the $z \leq 0.30$ bin, the type 2 quasar fraction is about 60% for $L_{[\text{OIII}]} = 10^{8.3}$ to $10^9 L_{\odot}$. For $z \leq 0.30$ and $0.30 < z \leq 0.50$, our strongest limits come from the highest luminosity bin, which constrain the type 2 quasar fraction to be at least 40% and 60% at $L_{[\text{OIII}]} \sim 5 \times 10^9 L_{\odot}$, respectively. Obscured quasar fractions derived from X-ray samples (at $z \sim 3$) are shown for comparison: Ueda et al. (2003; open squares), Grimes et al. (2004; open triangles), Hasinger (2004; open circles). Here, we convert the hard (2-10 keV) X-ray luminosities to [OIII]5008 luminosities by shifting by 1.59 dex following Heckman et al. (2005). Also shown are results from Simpson (2005; open diamonds), measured from a sample of SDSS DR2 objects with redshifts $0.02 < z < 0.30$. At face value, our lower limits on the type 2 fraction are consistent with measurements from the X-ray surveys, but in practice the type 2 quasar fraction may be significantly higher than our lower limits, as discussed above.

TABLE 1
CATALOG OF 887 OPTICALLY-SELECTED TYPE 2 QUASARS

RA	Dec	redshift	$L_{[\text{OIII}]}^{(\text{G})}$	$L_{[\text{OIII}]}^{(\text{NP})}$	Plate	Fiber	MJD	Tcode	$S_{20\text{cm}}$	RMS	u_{PSF}	g_{PSF}	r_{PSF}	i_{PSF}	z_{PSF}	σ_u	σ_g	σ_r	σ_i	σ_z
0.746236	0.671701	0.6007	9.04	9.12	686	350	52519	00001	0.00	0.149	21.67	21.35	20.54	19.72	19.83	0.36	0.05	0.04	0.03	0.11
0.965958	-1.028334	0.2689	8.16	8.15	669	289	52559	00001	8.45	0.148	21.93	20.68	19.26	18.84	18.31	0.20	0.03	0.02	0.02	0.03
1.222618	-0.843989	0.6430	9.18	9.20	669	209	52559	00001	0.00	0.153	22.37	21.90	21.03	20.19	19.97	0.32	0.11	0.06	0.04	0.13
1.870121	1.101123	0.4663	8.33	8.33	669	457	52559	00001	0.00	0.084	21.80	21.80	20.29	19.66	19.19	0.21	0.07	0.03	0.03	0.07
2.799806	0.940632	0.4094	8.67	8.66	669	602	52559	00001	0.00	0.117	21.89	21.10	19.84	19.19	18.99	0.30	0.06	0.03	0.02	0.06
2.862281	15.891562	0.0999	8.16	8.17	752	380	52251	10000	0.00	-1.000	20.72	19.28	18.50	17.88	17.61	0.09	0.02	0.02	0.02	0.03
3.026290	-9.790457	0.1668	8.54	8.55	652	399	52138	10000	0.00	0.153	20.42	18.95	18.16	17.81	17.69	0.07	0.02	0.02	0.02	0.03
5.070319	-9.545760	0.3600	8.60	8.62	1913	381	53321	00001	0.00	0.149	20.05	19.46	18.74	18.54	18.27	0.05	0.02	0.01	0.02	0.03
5.344129	-0.254834	0.5493	8.35	8.36	687	22	52518	00001	1.48	0.175	21.35	21.02	20.24	19.82	19.61	0.15	0.04	0.03	0.03	0.08
6.381066	-10.672835	0.3035	8.64	8.65	653	149	52145	01000	1.16	0.135	19.78	19.59	19.06	18.94	18.50	0.05	0.02	0.02	0.02	0.04

NOTE.—(1) RA and Dec are in J2000.0 coordinates.

(2) $L_{[\text{OIII}]}^{(\text{G})}$ and $L_{[\text{OIII}]}^{(\text{NP})}$ are listed in units of $\log(L/L_{\odot})$ and refer to Gaussian and non-parametric measures of the $[\text{OIII}]\lambda 5008$ line luminosity, respectively (§2.4).

(3) The first four digits of the target code (col. 9) show whether the object was targeted with the Galaxy, Low-z QSO, High-z QSO, or Serendipity FIRST algorithm, in that order. The last digit indicates whether the object belongs to the Special Southern survey.

(4) $S_{20\text{cm}}$ is the peak flux (in mJy/beam) of the nearest match within $2''$ from the FIRST survey (Becker et al. 1995), and is listed as zero, if there is no match. If the object is not in the FIRST survey area, the RMS flux value is listed as -1 .

(5) Columns 12-16 and 17-21 list *ugriz* PSF asinh magnitudes from the SDSS TARGET database, corrected for Galactic extinction (Schlegel et al. 1998), and their 1-sigma errors.

Table 1 is presented in its entirety in the electronic edition of the *Astronomical Journal*. A portion is presented here for guidance regarding its form and content.

TABLE 2
SDSS SPECTROSCOPIC TARGET ALGORITHMS

Target Algorithm	No. of Obj.
Main Survey	
Main Galaxy	366
Main Low-z QSO	76
Main High-z QSO	89
Main Serendipity FIRST	276
Main LRG	64
Main QSO FIRST	14
Main ROSAT	28
<i>Combined</i>	771
Special Southern Survey	
Southern Galaxy	4
Southern LRG	5
Southern Low-z QSO	20
Southern High-z QSO	6
Southern Serendipity FIRST	9
Southern ROSAT	1
Faint quasars	31
Photo-z	29
Faint LRG	5
<i>u</i> -band galaxy	2
<i>Combined</i>	116

NOTE.—SDSS spectroscopic target algorithms important for selecting type 2 quasars, and the number of objects targeted by each. Objects can be targeted by multiple algorithms, so these numbers do not add up to the total number of objects. The type 2 quasar luminosity function presented in this paper is derived from the 740 objects targeted by the top four Main target algorithms: Galaxy, Low-z QSO, High-z QSO and Serendipity FIRST.

TABLE 3
 MEAN V/V_{\max} VALUES CALCULATED FROM THE TYPE 1 AND TYPE 2 QUASAR SAMPLES.

	No.	$\langle V/V_{\max} \rangle$
Type 1 Quasars		
$0.00 < z \leq 0.30$	1020	0.55
$0.30 < z \leq 0.50$	2802	0.56
$0.50 < z \leq 0.83$	4181	0.57
Combined	8003	0.61
Type 2 Quasars		
$0.00 < z \leq 0.30$	420	0.46
$0.30 < z \leq 0.50$	175	0.61
$0.50 < z \leq 0.83$	145	0.54

NOTE.—Mean V/V_{\max} values calculated from the type 1 and type 2 quasar samples for three redshift ranges: $z \leq 0.30$, $0.30 < z \leq 0.50$ and $0.50 < z \leq 0.83$. For a uniformly-selected, non-evolving population of objects, $\langle V/V_{\max} \rangle$ is expected to be 0.5. Our type 1 quasar sample is complete and values greater than 0.5 indicate that there is positive redshift evolution within each redshift range. Our type 2 quasar sample is incomplete and the deviation of $\langle V/V_{\max} \rangle$ from 0.5 is due to a combination of redshift evolution and selection effects, which we do not attempt to disentangle.